Porphyry Cu–Au ± Mo mineralization hosted by potassic igneous rocks: implications from the giant Peschanka porphyry deposit, Baimka Trend (North East Siberia, Russia)

Andrey F. Chitalin[1]*, Ivan A. Baksheev[2], Yurii N. Nikolaev[2], Georgy T. Djedjeya[2], Yuliya N. Khabibullina[2] and Daniel Müller[3]

[1]Institute of Geotechnology, MSU Science Park 1, Leninskie Gori, Bld 77, 119234, Moscow, Russia

[2]Moscow State University, Geological Department, 119234, Leninskie Gori, 119234, Moscow, Russia

[3]Consulting Geologist, Las Condes, Santiago, Chile

AFC, 0000-0003-3998-5372; IAB, 0000-0001-6920-427X; YNK, 0000-0003-2544-7776; DM, 0000-0002-0933-0394

*Correspondence: achitalin@yandex.ru

Abstract: Porphyry Cu–Au ± Mo mineralization at Peschanka is hosted by monzodiorite and monzonite intrusions with high-K calc-alkaline to shoshonitic compositions and dated at about 144.1 ± 1.5 Ma, using U/Pb zircon ages. The Cretaceous intrusions are emplaced in a melange of Cretaceous island arcs, a tectonic setting comparable with other world-class porphyry Cu–Au deposits, such as Oyu Tolgoi, Mongolia and Pebble, Alaska. Abundant primary magnetite contents of the Peschanka intrusions, as well as numerous gypsum and anhydrite veins, reflect the high oxidation states of their parental magmas. This mineralogical interpretation is confirmed by high whole-rock Fe_2O_3/FeO ratios and high V/Sc ratios of the rocks of up to 1.27 and up to 21.9, respectively. The whole-rock Eu/Eu* ratios of the Peschanka intrusions are ≥1 which is also typical for potassic igneous rocks with high oxidation states. Abundant amphibole and biotite phenocrysts of the intrusions as well as their high whole-rock Sr/Y ratios of up to 225 document significantly high H_2O contents of the high-K magmas. Peschanka contains a resource of >9.5 Mt of copper at an average grade of 0.43 wt% and 16.5 Moz of gold at a high average grade of 0.23 g/t and thus represents one of the largest undeveloped greenfield copper projects worldwide. The vicinity of Peschanka still offers significant brownfield exploration potential. The hypogene vein-related and disseminated Cu–Au ± Mo sulfide mineralization at Peschanka is structurally controlled by significant NE-trending strike-slips that acted as the conduits for the hydrothermal fluids. The central part of the orebody consists of high-grade north–south-trending sheeted quartz–bornite veining with unusually high vein densities. The highest Cu and Au grades are directly correlated with high vein densities. Peschanka is defined by distinct hydrothermal alteration zones including potassic, phyllic, propylitic and argillic assemblages, but a distinct lack of advanced argillic alteration. The mineralization itself is also zoned ranging from a central Mo–Cpy–Bn sulfide assemblage to a peripheral Py–Mt-dominated zone ('pyrite-shell'). Late-stage polymetallic assemblages overprint and surround the main stockwork zone.

For several decades, the parental intrusions hosting economic porphyry Cu–Au deposits have been assigned to 'normal' calc-alkaline magmatic systems (e.g. Sillitoe 1972, 1973; Titley 1972, 1975, 1981; Bouse *et al.* 1999). However, modern studies reveal the increasing role of high-K intrusions in mineral exploration (Mutschler and Mooney 1993; Müller and Groves 1993; Sillitoe 1997; Müller 2002; Sillitoe 2002; Soloviev 2014). Numerous world-class porphyry copper–gold and epithermal gold deposits worldwide are hosted by high-K calc-alkaline or shoshonitic intrusions (cf. Müller and Groves 2019).

This paper documents the world-class Peschanka porphyry Cu–Au ± Mo deposit in the Baimka Mineralized Trend, NE Siberia or NE Russia, and discusses its structural framework, tectonic setting, hydrothermal alteration and mineralization as well as elucidating the important role of its parental high-K monzonitic intrusions. Peschanka is an example of copper–gold mineralization hosted by H_2O-rich potassic intrusions with high oxidation states, comparable with Grasberg, Indonesia (Pollard and Taylor 2002), Oyu Tolgoi, Mongolia (Crane and Kavalieris 2012) and Pebble, Alaska (Olson *et al.* 2017). It probably represents the most isolated copper–gold deposit of significant grade and tonnage worldwide (Chitalin *et al.* 2012; Marushchenko *et al.* 2015, 2018). The Baimka Trend comprises a

From: Krmíček, L. and Chalapathi Rao, N. V. (eds) *Lamprophyres, Lamproites and Related Rocks: Tracers to Supercontinent Cycles and Metallogenesis*. Geological Society, London, Special Publications, **513**, https://doi.org/10.1144/SP513-2020-178

cluster of porphyry copper–gold systems. The best explored one to date is Peschanka, which crops out at the surface and is well defined by systematic deep diamond drilling (Chitalin *et al.* 2012). Peschanka represents the largest porphyry Cu–Au ± Mo deposit in Russia, comprising a resource of >9.5 Mt of copper and 16.5 Moz of gold, and it ranks in the top 10 undeveloped greenfield copper projects worldwide (https://www.kazminerals.com/repository/news-container/news/2018/kazminerals-acquires-baim skaya-copper-project

Geological setting

Regional tectonics

The main tectono-magmatic units of the Verkhoyansk–Chukotka Mesozoides are shown in Figure 1. The following evolutionary stages are documented: (1) destruction of the North Asian continental plate during the Paleozoic (Ordovician to Triassic); (2) amalgamation and collision of paleaoisland arcs during the Middle Mesozoic (Middle Jurassic to Mid-Cretaceous for the Koryak terranes); and (3) continental growth during the Late Mesozoic and Early Tertiary (Cretaceous to Middle Eocene). The formation of the accreted terranes was mainly controlled by the collision between the North Asian continental plate and the Kolyma–Omolon and Chukotka microcontinents (Parfenov *et al.* 2009; Sokolov 2010).

The Chukotka fold belt comprises two tectonic units, the Anyui–Chukotka fold system (i.e. Chukotka microcontinent) and the South Anyui suture zone. The latter is the product of the collision between the Chukotka microcontinent and the

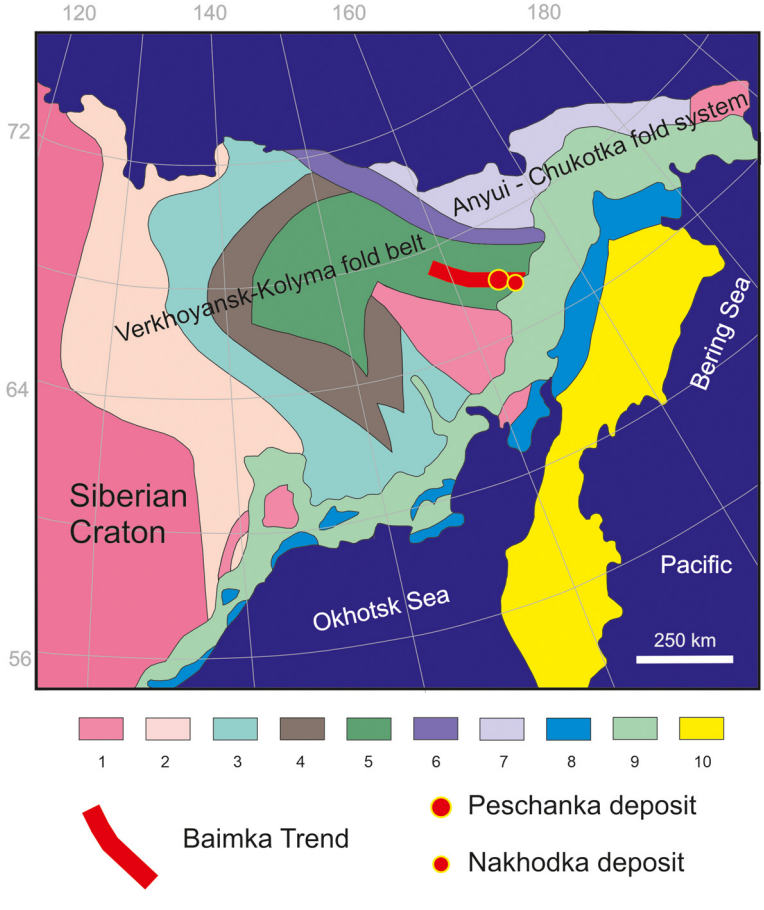

Fig. 1. Tectonic sketch map of northeastern Russia (simplified after Sokolov 2010) showing the location of the Baimka trend and related porphyry–Cu–Au deposits: (1) Siberian Craton and cratonic terranes; (2) Verkhoyansk terrane; (3) Yana–Kolyma terrane; (4) Paleozoic terranes; (5) Alazeya–Oloy fold system; (6) South-Anyui Suture; (7) East Chukotka terrane; (8) Late Jurassic magmatic belt; (9) Okhotsk–Chukotka Cretaceous magmatic belt; and (10) Koryak–Kamchatka fold belt.

Siberian continental margin (i.e. the Verkhoyansk–Kolyma fold belt; cf. Sokolov *et al.* 2011, 2015).

Two main stages of the geological evolution of the South Anyui Suture (Fig. 1) are distinguished: (1) the oceanic stage during the Paleozoic to Late Jurassic, which was dominated by the large Proto-Arctic ocean including local ensimatic palaeoisland arcs; and (2) the collisional stage during the Late Jurassic to Early Cretaceous, which was defined by the subduction of the paleao-ocean as well as the formation of the South Anyui turbidite basin and a fold–nappe structure during the Hauterivian–Barremian period. During collision, the oceanic and island-arc complexes were thrust towards the north and onto the passive margin of the Chukchi Peninsula. The thrusting was followed by subsequent strike-slip faulting and the formation of south-vergent overthrust sheets. During the Aptian–Albian period, collision gave way to an extensional phase documented by the formation of metamorphic core complexes and orogenic basins (Sokolov *et al.* 2015).

The West Chukotka area comprises four major tectono-magmatic elements, which are from the SW to the NE (see also Fig. 2): (1) the Omolon cratonic terrane; (2) the Oloy zone, dominated by Jurassic and Early Cretaceous continental arc magmatism; (3) the South Anyui suture zone, formed during the Early Cretaceous and after the closure of the oceanic basin by subsequent collision between the Chukotka block and the Siberian craton; and (4) the Anyui zone, representing the former passive margin of the Chukotka block (Parfenov 1991; Nokleberg *et al.* 2001). All four zones are overprinted by a post-collisional magmatic event dated at about 121–112 Ma (Tikhomirov *et al.* 2017; Kara *et al.* 2019) and, subsequently, by subduction-related volcanism along the Okhotsk–Chukotka volcanic belt dated at about 106–74 Ma (Akinin and Miller 2011; Tikhomirov *et al.* 2012).

Most porphyry-style deposits of the Verkhoyansk–Kolyma fold belt are situated in either the Magadan or the West Chukotka regions. The Oloy zone hosts the large Cretaceous Peschanka and Nakhodka porphyry Cu–Au ± Mo deposits, as well as the smaller Mangazeika porphyry Cu–Mo–Au and the Klen intermediate sulfidation epithermal gold deposits (Nikolaev *et al.* 2020). The large Karalveem intrusion-related gold deposit is situated within the Anyui tectonic zone (Kondratiev *et al.* 2017). The South Anyui suture zone hosts the Kekura intrusion-related gold deposit deposit (Nagornaya *et al.* 2020).

Geology of the Baimka Trend

The large Peschanka porphyry Cu–Au ± Mo deposit, the Nakhodka ore field and several smaller porphyry Cu–Au and epithermal Au prospects occur within the Oloy tectonic zone, which is locally also known as the Baimka Trend. The Baimka Trend has a NW-orientation with a length of approximately 200 km and a width ranging between 25 and 50 km. It is structurally controlled by the regional Baimka Shear Zone (Fig. 3; Chitalin *et al.* 2013, 2016). All mineral deposits and occurrences are spatially associated with high-K monzonite intrusions of the Early Cretaceous Egdykgych Complex. The U/Pb zircon age of monzodiorite hosting mineralized and barren stockworks at Peschanka is about 144.1 ± 1.5 Ma (A. Chitalin *et al.*, unpublished data). This age confirms the previously reported age of about 142 Ma (cf. Moll-Stalcup *et al.* 1995).

The Baimka Shear Zone was formed in two stages during the Late Jurassic to Early Cretaceous (Chitalin 2019). During the first stage, NW-trending sinistral strike-slip and reverse faults were formed in relation to a regional left-lateral shear zone (Fig. 3). The Late Jurassic (*c.* 150 Ma) composite Egdykgych pluton was intersected and displaced along this sinistral strike-slip fault. During the second stage, the Baimka zone was re-activated as a right-lateral shear zone. This phase is documented by secondary extensional structures, normal faults and strike-slip faults. Extensional structures within this large shear zone controlled the emplacement of the Early Cretaceous intrusions and associated porphyry Cu–Au ± Mo deposits. Auriferous epithermal Au veins and sheeted vein zones mainly developed along dextral strike-slip and conjugated sinistral strike-slip faults. Strike-slip movements and associated thrust faults were active at least until the Albanian. Low-angle thrust faults with cataclastic textures intersect stockwork mineralization at the Nakhodka porphyry Cu–Au deposit (Chitalin *et al.* 2016; Chitalin 2019).

Exploration history of the Peschanka porphyry Cu–Au ± Mo deposit

The Peschanka porphyry Cu–Au–Mo deposit is situated in western Chukotka, Siberia, about 250 km to the SW of the town of Bilibino. The deposit was discovered in 1973 and explored during the late 1970s and 1980s. The main features of the geology and mineralization of Peschanka were originally published by Migachev *et al.* (1985). Follow-up exploration was carried out during 2009–19 by the Baimka Mining Company under the guidance of the Regional Mining Company, LLC. In late 2019, KAZ Minerals acquired the Baimka Copper Project and commenced its development for production. Owing to the high exploration potential for satellite porphyry Cu–Au orebodies, KAZ Minerals also conducts an extensive brownfields exploration programme.

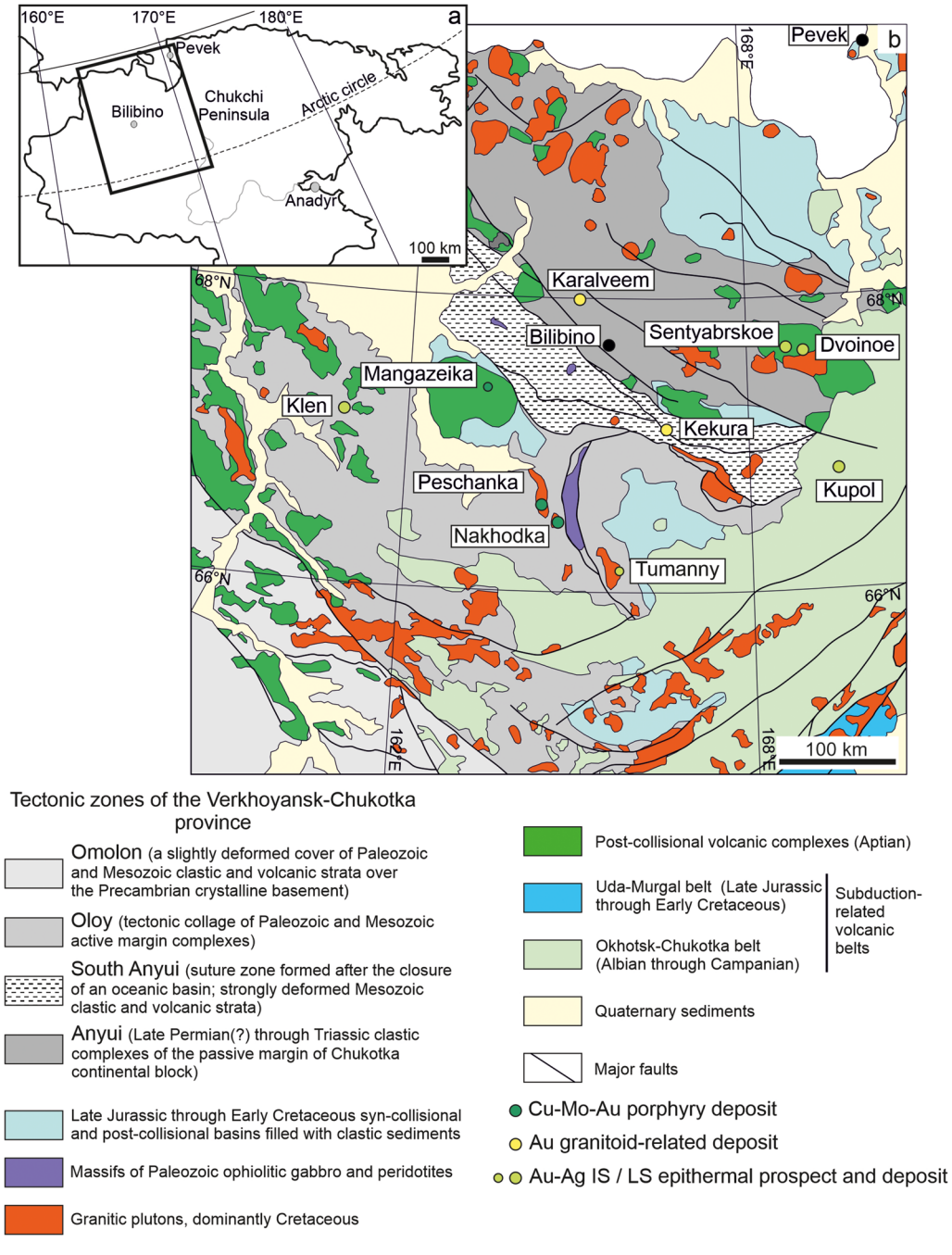

Fig. 2. (**a**) Geographic location map of Siberia; and (**b**) Tectonic sketch map of Western Chukotka; modified after Tikhomirov *et al.* (2017).

Geological overview

The deposit is located at the eastern part of the Early Cretaceous Egdygkych composite pluton, consisting of monzogabbros, diorites and monzodiorites, that are locally intruded by smaller quartz–monzodiorite and syenite porphyries. The porphyry intrusions represent about 10–15 vol% of this large pluton

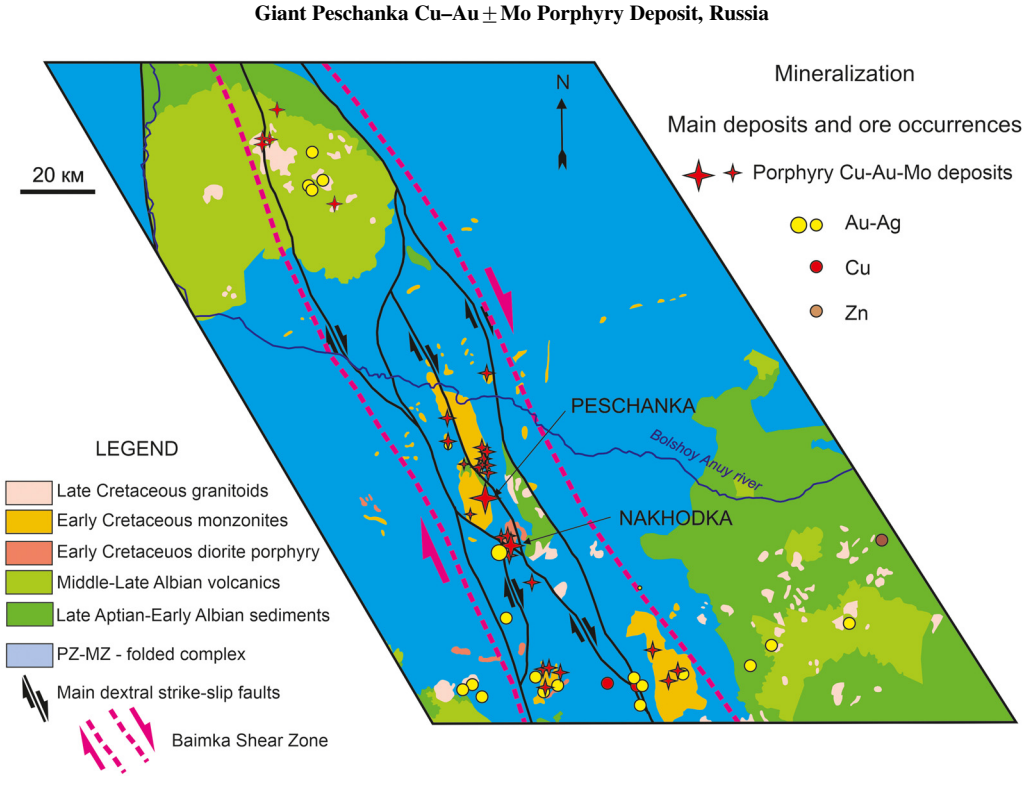

Fig. 3. Magmatism and associated mineral deposits of the Baimka Trend.

(Chitalin *et al.* 2012, 2013; Marushchenko *et al.* 2018). The Peschanka porphyry deposit comprises a north–south-trending zone containing veinlet–stringer and disseminated ore-grade mineralization, measuring about 7000 m along-strike and up to 1500 m in width, locally referred to as 'linear stockwork' (Fig. 4). The veinlets make up a tight sheeted veining and stockwork zone in the central part of the deposit. A net-like structure of the stockwork with up to six overprinting veinlet systems is documented. The earlier hematite–magnetite, magnetite and quartz–magnetite veinlets are cut by late-stage quartz–sulfide veinlets.

The quartz–sulfide linear stockwork is structurally controlled by a major dextral strike-slip fault and locally intersected by large NE-trending structures dividing it into three sectors (Fig. 4).

Hydrothermal alteration zones

The igneous rocks are overprinted by significant propylitic, potassic, phyllic and argillic alteration zones. The outline of the stockwork orebody directly overlaps with potassic (biotite–magnetite–K-feldspar) alteration assemblages. The propylitic alteration zone is typically composed of epidote–actinolite–chlorite–albite–magnetite ± tourmaline assemblages defining an area of up to 1 km around the potassic core. In places, a late-stage quartz–sericite–pyrite ± chlorite ± albite ± dolomite (phyllic) alteration is superimposed onto the early-stage propylitic and potassic alteration assemblages. The phyllic alteration assemblage includes quartz–sulfide veining (Fig. 5) and its spatial distribution is usually structurally controlled by strike-slip structures as well as thrust and normal faults. Locally, the late-stage phyllic alteration zones contain enclaves with relics of the original potassic and/or propylitic alteration assemblages. Structurally controlled phyllic alteration zones vary in thickness between 1 mm and >20 m, extending along-strike for tens or, locally, even hundreds of metres. The NE-trending strike-slip structures are typically associated with phyllic alteration that overprints the original potassic alteration assemblage. Potassic alteration occurs both as pervasive and as structurally controlled.

Locally, the monzonites are intersected by quartz–sericite–pyrite–kaolinite crackle veins composed of quartz–sericite altered angular monzonite clasts cemented by clay minerals (Fig. 6b). These zones locally contain large euhedral recrystallized pyrite grains.

Potassic alteration assemblages typically comprise a reddish fine- to medium-grained mineralogy

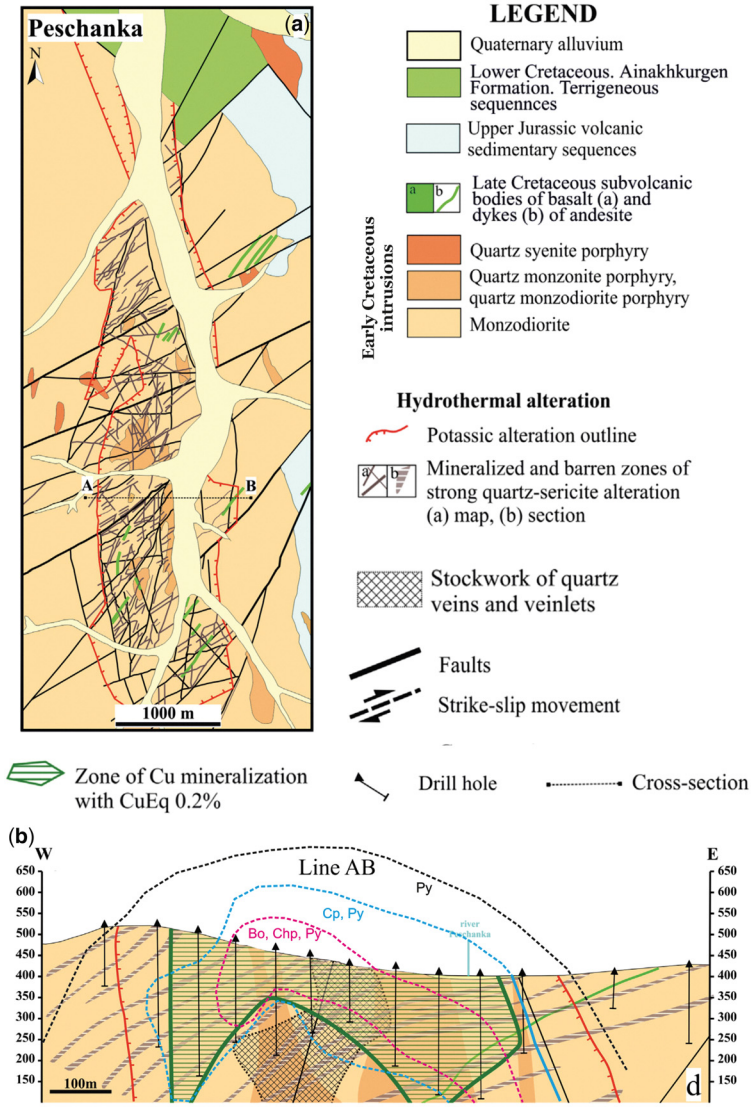

Fig. 4. Simplified geological map (**a**) and cross-section (**b**) of the Peschanka deposit.

consisting of hydrothermal biotite, potassic feldspar, magnetite and quartz (Fig. 7a). This alteration type is locally overprinted by quartz–sericite alteration and primary textures are retained as relicts in places. Biotite occurs as dark and light brown isolated plates or their clusters. Dark brown biotite is relict magmatic. Primary magmatic biotite has high TiO_2 contents and high $Fe_{tot}/(Fe_{tot} + Mg)$ ratios of up to 5.3 wt% and up to 0.36, respectively. In monzodiorite intrusions, primary magmatic biotite is commonly associated with magnesio-hastingsite, diopside and titanomagnetite with exsolved ilmenite lamellae indicating high oxidation states of the parental magma. In contrast, the light brown biotite is recrystallized hydrothermal. Titanium contents and $Fe_{tot}/(Fe_{tot} + Mg)$ ratios of the hydrothermal mica are 0.9–3.8 wt% and 0.16–0.34, respectively. The lowest TiO_2 content of 0.33 wt% and a $Fe_{tot}/(Fe_{tot} + Mg)$ ratio of 0.19 are recorded in hydrothermal phlogopite. Potassic feldspar occurs as small irregular grains commonly replacing magmatic K–Na feldspar and developing in paragenesis with albite and quartz. In places, large hydrothermal segregations of zoned potassic feldspar grains occur. In contrast to

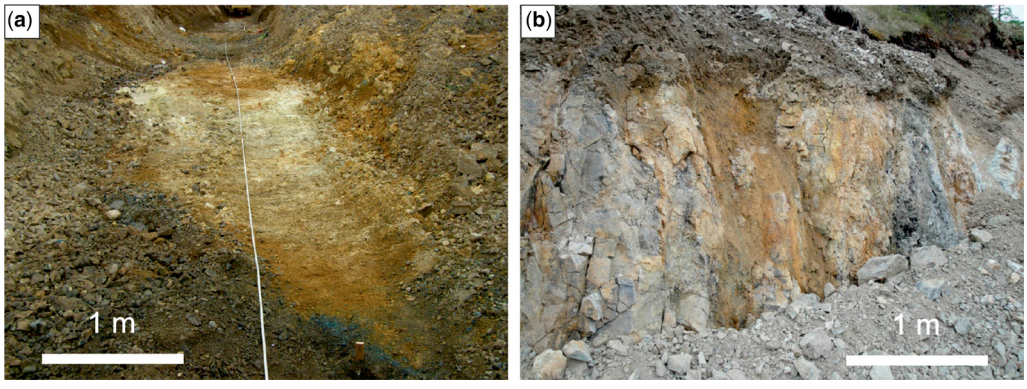

Fig. 5. Trench exposures of strong quartz–sericite ± pyrite alteration overprinting potassic altered monzodiorite intrusions: (**a**) at the bottom of a trench and (**b**) in the wall of a trench.

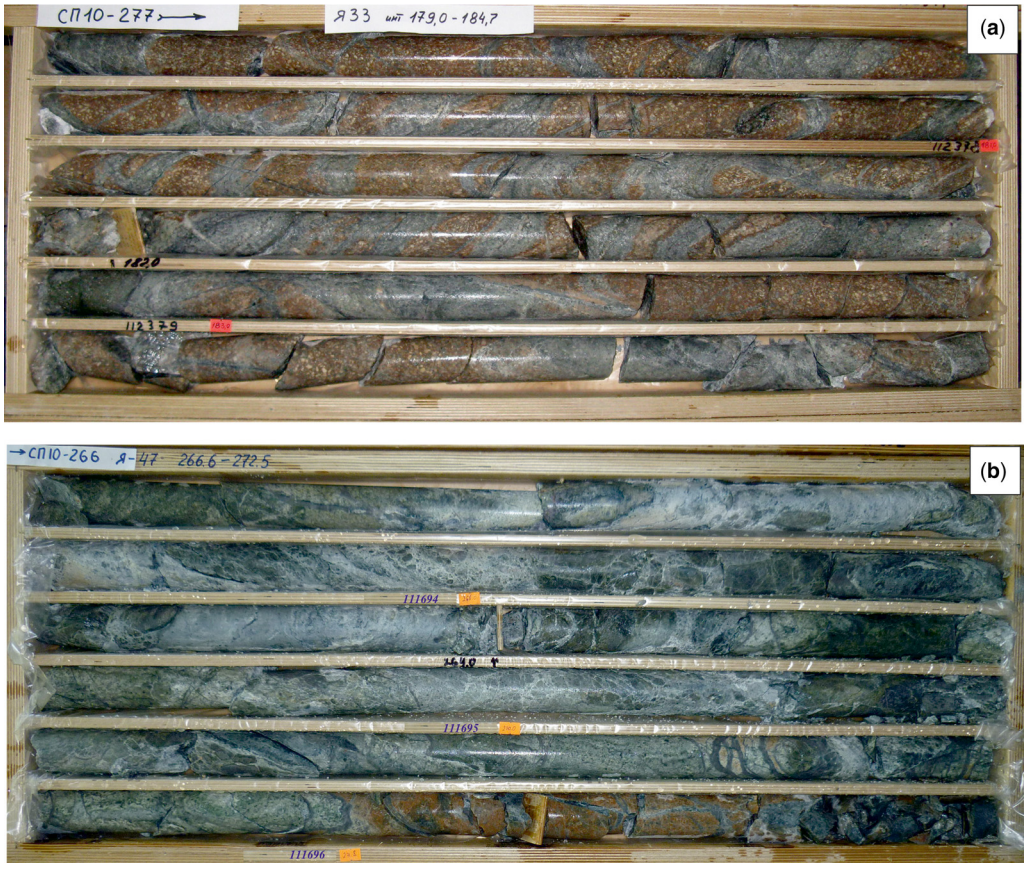

Fig. 6. Drillcore intervals from mineralized and potassic altered monzonite porphyry intersected by: (**a**) sheeted sericite–pyrite veining and associated phyllic alteration; and (**b**) cataclastic quartz–sericite–pyrite-kaolinite crackle veining.

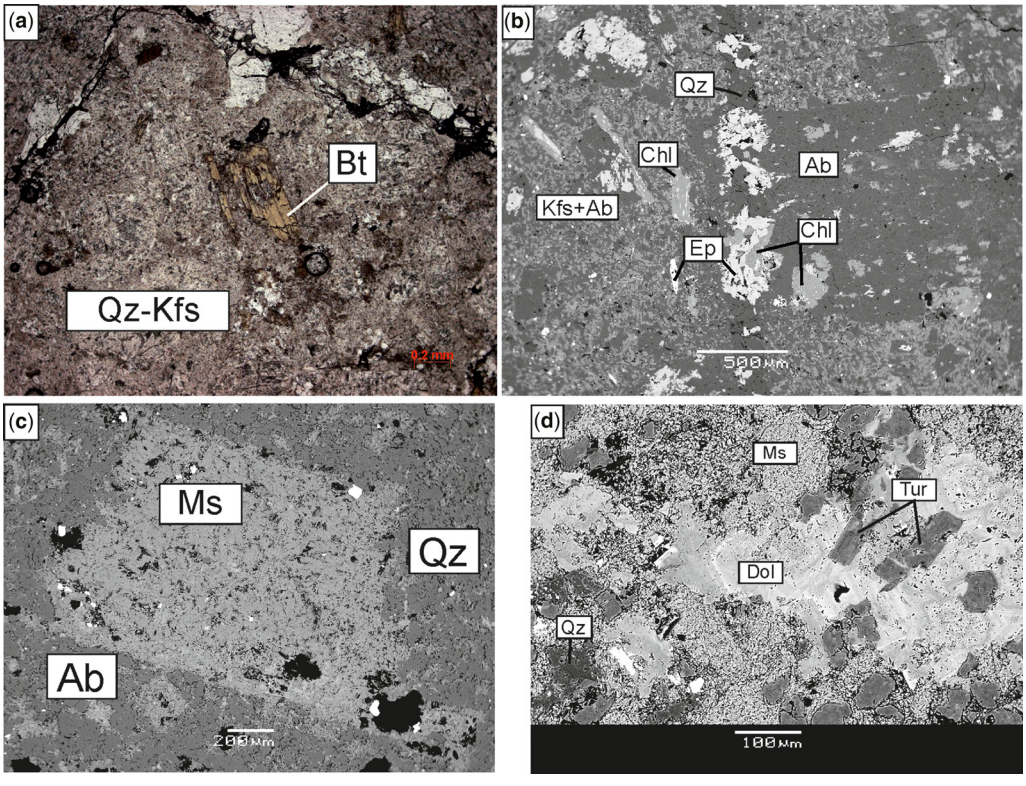

Fig. 7. Photomicrograph (a, plane polarized light) and back-scattered electron images (b–d) of altered rocks at the Peschanka deposit. (**a**) Potassic alteration – phenocryst of light brown hydrothermal biotite in the fine-grained quartz-potassic feldspar matrix; (**b**) propylitic alteration composed of quartz, fine-grained albite–potassic feldspar aggregate, epidote and chlorite, the latter containing titanite inclusions; (**c**, **d**) phyllic alteration – (c) quartz–albite–muscovite assemblage and (d) tourmaline–quartz–dolomite–muscovite assemblage. Mineral abbreviations: Ab, albite; Bt, biotite; Chl, chlorite; Dol, dolomite; Ms, muscovite; Qz, quartz; Tur, tourmaline.

magmatic K–Na feldspar containing BaO concentration of <3.7 wt% BaO, the hydrothermal potassic feldspar has high BaO content of up to 7.3 wt%.

Propylitic alteration assemblages are reported in detail by Marushchenko (2013) and thus we only provide a brief description of this alteration type. Dark green propylitic altered rocks are composed of epidote, albite, quartz, actinolite, tourmaline, chlorite and calcite (Fig. 7b). In places, there is abundant epidote and the rocks are light green. Accessory minerals are rutile and titanite. Opaque minerals are magnetite and, locally, rare pyrite. Epidote either occurs as individual light green phases or as monomineralic aggregates commonly in veinlets up to 0.5 cm thick. It usually replaces primary plagioclase and, less frequently, diopside, amphibole and biotite. Epidote is locally replaced by late-stage calcite or cut by calcite veinlets. The epidote crystals are complexly zoned owing to variable Fe concentration. Amphiboles can be assigned to two different generations: (1) early-stage magnesio-hornblende that commonly replaces primary clinopyroxene and is locally intergrown with epidote, with the mg# value ($Mg/(Mg + Fe^{2+})$) of the magnesio-hornblende varying between 0.78 and 0.95; and (2) late-stage tremolite–actinolite solid solution with the mg# value between 0.60 and 0.92 and replacing both magnesio-hornblende and primary clinopyroxenes. Tourmaline typically occurs as spherulitic aggregates consisting of small dark green phases. Fractures intersecting these tourmaline aggregates are healed by quartz and sericite, and locally by sericite–potassic feldspar–chlorite assemblages with rare chalcopyrite and galena, which are interpreted as late-stage epithermal overprints. Electron microscopic study revealed a complex zoning of individual tourmaline crystals owing to different Fe contents. The mineral chemistry implies that the tourmalines belong to the oxy-dravite–bosiite solid solution series, which is typical for tourmalines in

the vicinity of porphyry Cu–Au deposits (Baksheev *et al.* 2012). Chlorite aggregates are typically zoned with Fe-rich rims and Mg-rich cores. Based on the mineral chemistry, the chlorite can be classified as clinochlore. Propylitic alteration contains magnetite without ilmenite lamellae and pyrite.

Phyllic alteration assemblages are documented in detail by Marushchenko *et al.* (2015) and, hence, this paper only provides a brief description. Quartz–sericite altered rocks are commonly light grey and they retain relict porphyritic textures, in places. Phyllic alteration consists of hydrothermal muscovite, phengite and quartz as the main minerals (Fig. 7c), with chlorite, albite and tourmaline as minor constituents. Rutile and apatite are accessory minerals. Muscovite and phengite are intimately intergrown with albite and tourmaline or replacing chlorite and potassic feldspar. Muscovite is more abundant than phengite. Chlorite occurs as fine flakes; the chlorite is typically zoned with Fe-depleted rims and, in places, it is accompanied by sulfides. The chlorite can be defined as chamosite and clinochlore. Tourmaline occurs as light green isolated grains or clustering in radial aggregates or rosettes. Electron microscopic study revealed that the tourmaline belongs to the oxy-dravite–dravite solid solution series, which is a typical composition of tourmalines from phyllic alteration zones in porphyry Cu–Au deposits (Baksheev *et al.* 2012). In addition, there is tourmaline–muscovite–dolomite–quartz rock (Fig. 7d), which is associated with quartz–dolomite-veinlets containing polymetallic mineralization.

Argillic alteration assemblages are local and rare at Peschanka. Kaolinite alteration is locally recorded in trenches or intersected in drillcore and it is typically structurally controlled. There is no evidence for advanced argillic alteration at Peschanka and a distinct lack of alteration minerals such as alunite, pyrophyllite and andalusite.

Mineralization assemblages

Two mineralization assemblages can be distinguished at Peschanka: (1) a main and early-stage porphyry Cu–Au ± Mo mineralization (Figs 8, 9 & 10a–c) and (2) a late-stage and mainly vein-related carbonate–polymetallic assemblage (Figs 10d–l & 11). The late-stage mineralization is frequently telescoped. The early-stage assemblage mainly consists of bornite, chalcopyrite, molybdenite and native gold. Sulfosalts such as tetrahedrite solid solution are very minor. In contrast, the second assemblage comprises pyrite, galena, sphalerite, chalcopyrite, tetrahedrite solid solution and, more rarely, hessite, petzite, tetradymite, altaite and goldfieldite. In places, but very rarely, enargite is documented in association with fahlore and chalcopyrite. Although this late-stage mineral assemblage is similar to high-sulfidation epithermal assemblages, it is accompanied by quartz–carbonate–phengite–muscovite ± tourmaline alteration. Importantly, no advanced argillic alteration assemblages are documented at Peschanka. Post-mineral calcite, gypsum and anhydrite veinlets are common (Fig. 9f). Supergene mineralization in the oxidation zone comprises copper carbonates and sulfates, copper wad and less frequent covellite; the chalcocite-group minerals are rare.

Early-stage porphyry copper–gold–molybdenum mineralization:. Sulfides are distributed within grey-glassy quartz veins or along their margins, as well as in microfractures and cataclastic zones with fracture fill of hydrothermal chalcopyrite, bornite, molybdenite, pyrite, white quartz and calcite. Vertical, inclined and horizontal quartz-sulfide and barren quartz veinlets are documented within the stockwork (Fig. 8a & c). The central part of the stockwork zone includes high-grade subvertical and north–south-trending sheeted quartz–bornite vein zones (Fig. 8b & d). The vein density locally reaches 300 veinlets per metre in these sheeted vein zones and contains high grades of Cu and Au. The vein thickness is typically <1 mm. This sheeted vein mineralization is interpreted as the product of near-horizontal extensional tectonics. Hydraulic fracturing under excess pressures of the hot hydrothermal solutions could also have facilitated the intense sheeted veining. The early-stage hypogene vein-hosted and disseminated Cu–Au–Mo sulfide mineralization at Peschanka is controlled by significant NE-trending strike-slip structures that acted as the conduits for the hydrothermal fluids and resulted in the formation of a distinct sheeted and reticulate veining network spatially associated with a phyllic alteration overprint.

The major hypogene ore minerals are bornite, chalcopyrite and molybdenite with minor tetrahedrite solid solution (Marushchenko *et al.* 2018). Bornite commonly is intergrown with chalcopyrite and, in places, contains exsolution lamellae of chalcopyrite (Fig. 10a), which is quite common at gold-rich porphyry copper deposits (e.g. Northparkes, Australia: Müller *et al.* 1994). The mineral also contains inclusions of native gold (Fig. 10b), clausthalite, hessite and rare froodite. Bornite is mainly recorded from the hypogene potassic core of the deposit, which grades outwards through zones dominated by bornite–chalcopyrite, chalcopyrite and chalcopyrite–pyrite assemblages into a peripheral pyrite-dominated shell (see also Fig. 4b). Chalcopyrite occurs either as individual grains in association with molybdenite or as fine lamellae within bornite. Individual chalcopyrite grains are locally replaced by minor fahlores. In places, chalcopyrite is documented in late-stage veinlets (Fig. 11). However,

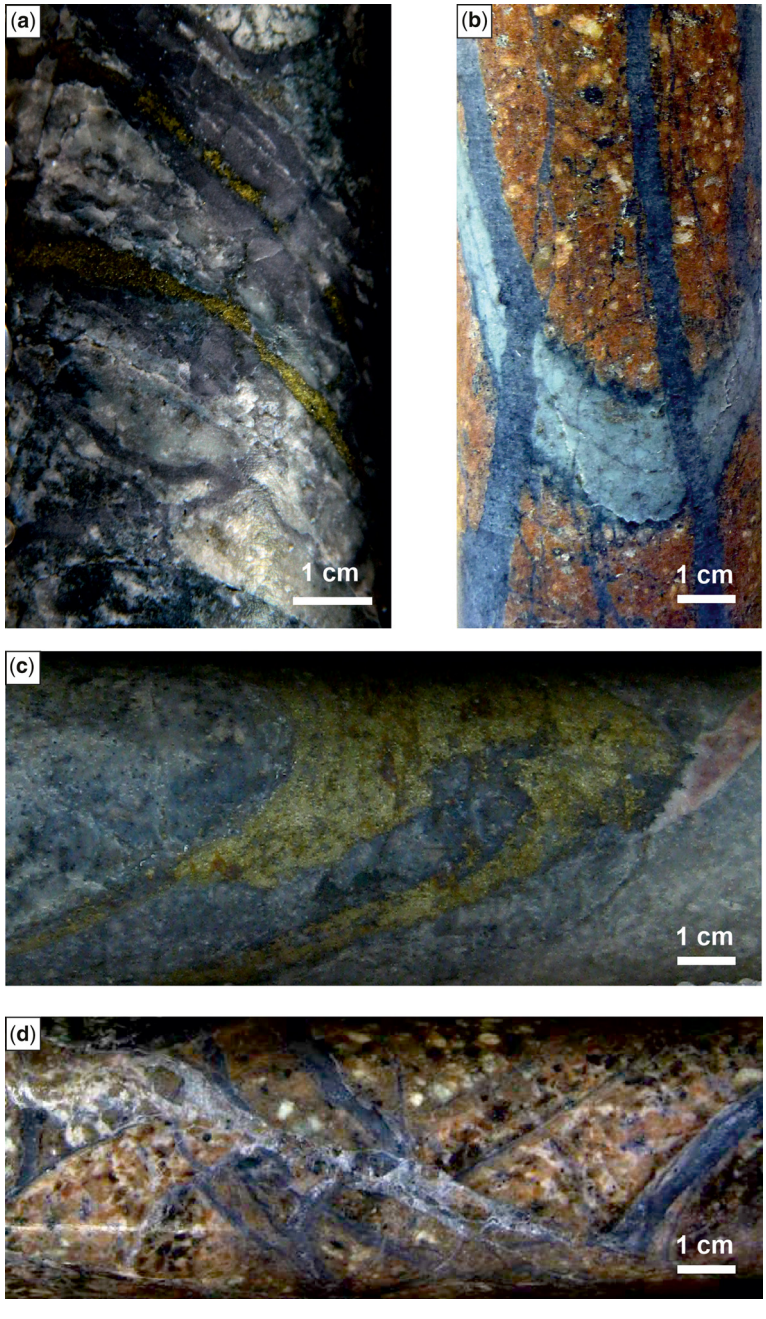

Fig. 8. Different vein types at the Peschanka deposit: (**a**) strongly Qtz–Ser altered monzonite porphyry intersected by quartz veining and cross-cutting Cpy veinlets; (**b**) Qtz–Ser zones cut by Qtz–Py veining in potassic altered monzonite porphyry; (**c**) Cpy veinlets in Qtz–Ser altered monzonite; and (**d**) grey Qtz–Mo veinlets cut by late-stage Qtz–Cc crackle vein, both hosted by monzonite porphyry. Ser = sericite, Cpy = chalcopyrite, Cc = chalcocite, Py = pyrite.

chalcopyrite and bornite are commonly distributed along the margins of glassy-grey quartz veins and veinlets, as well as in microfractures and breccia zones (Figs 8c & 9c–e). Molybdenite either occurs as small books or individual flakes in association with chalcopyrite and pyrite, or is finely disseminated

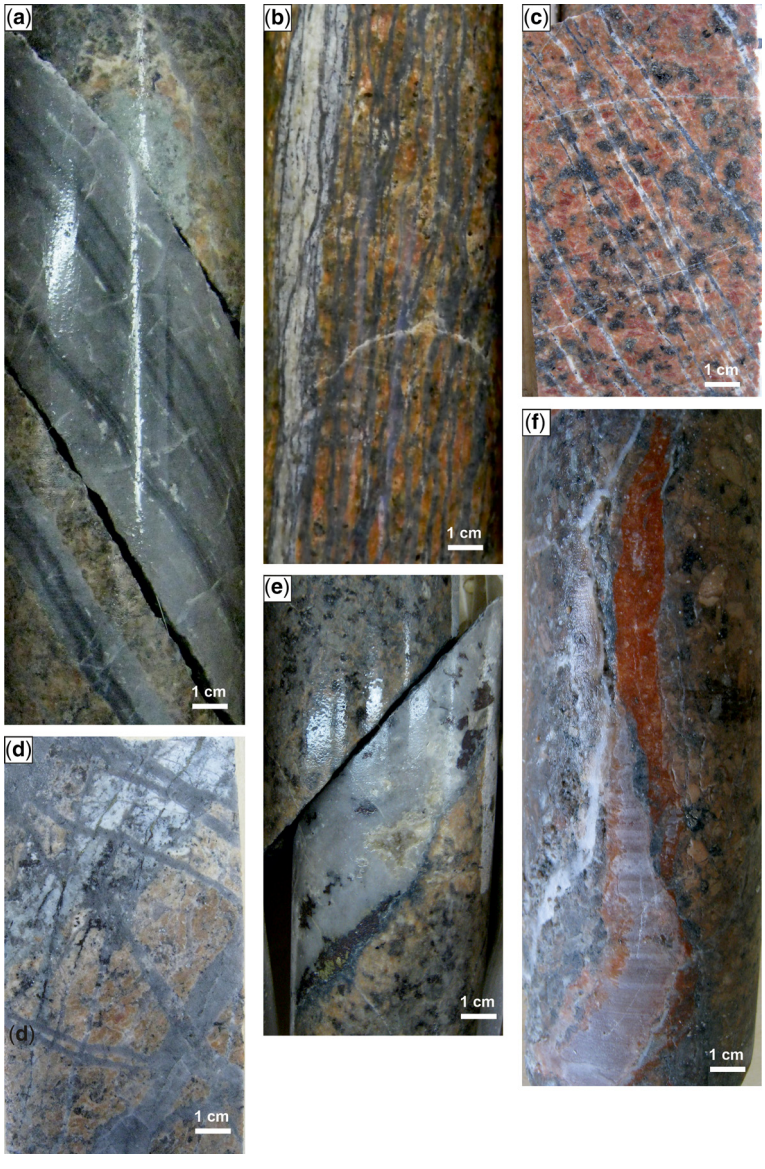

Fig. 9. Drill core samples of syn- and post-mineral veining: (**a**) banded grey Qtz–Mo veining with dark grey layers containing fine-grained disseminated molybdenite; (**b**) sheeted quartz veining and Qtz–Ser altered structure cutting potassic altered monzonite porphyry – note the white late-stage cross-cutting Cc veinlet; (**c**) grey sheeted Qtz veinlets containing disseminated bornite cutting potassic altered monzodiorite intrusion – note the white late-stage cross-cutting Qtz-Cc veinlets; (**d**) various generations of grey Qtz veinlets containing disseminated bornite and cutting potassic altered monzodiorite; (**e**) high-grade grey Qtz vein with lenses of bornite and chalcopyrite cutting potassic altered monzodiorite porphyry – the pink zone adjacent to the footwall of the vein is hydrothermal potassic feldspar; (**f**) complex multiphase post-mineral gypsum–anhydrite–calcite vein cutting potassic altered monzonite porphyry.

in quartz veins. It typically occurs in locally laminated, grey quartz dilation veinlets (Figs 8d & 9a), which form up to six intense vein systems with different orientations and vein densities of up to 60 veins/m in the central part of the deposit. The mineral has high Re content ranging from 1260 to 2670 ppm.

Fahlore, native gold and pyrite are minor constituents of the early-stage assemblage. Tetrahedrite

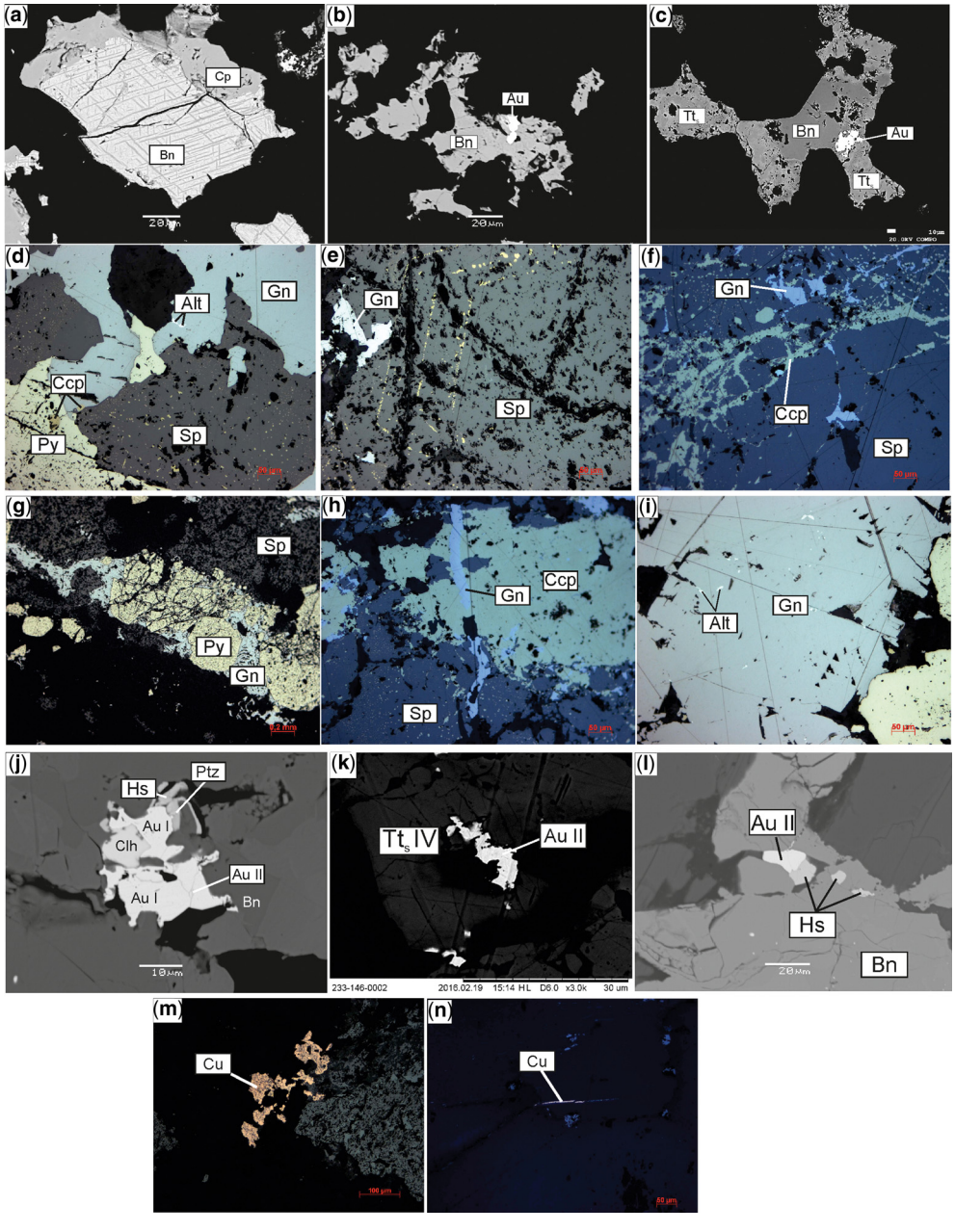

Fig. 10. Photomicrographs and back-scattered electron images of ore minerals from the Peschanka deposit. (**a**) Bornite with exsolution chalcopyrite lamellae intergrown with chalcopyrite; (**b**) microinclusions of native gold in bornite; (**c**) native gold embedded in tennantite–tetrahedrite, which partially replaces bornite; (**d**) intergrowth between sphalerite containing fine-grained disseminated chalcopyrite and galena containing inclusions of altaite and pyrite; (**e**) chalcopyrite inclusions aligned along growth zones of sphalerite crystal; (**f**) fractures within sphalerite filled with chalcopyrite and galena; (**g**) galena cement fractured pyrite crystals; (**h**) galena stringer vein cutting chalcopyrite and sphalerite; (**i**) altaite inclusions in galena; (**j**) first-generation gold overgrowing clausthalite, overprinting by petzite and hessite and cutting by stringers of gold II; (**k**) second-generation gold along fractures within tennantite IV; (**l**) intergrowth of gold II and hessite in the interstices between bornite grains; (**m**) native occurring as pockets; and (**n**) native copper fill fracture. Mineral abbreviations: Alt, altaite; Au, native gold; Bn, bornite; Ccp, chalcopyrite; Clh, clausthalite; Gn, galena; Hs, hessite; Ptz, petzite; Py, pyrite; Sp, sphalerite; Tt_s, tetrahedrite solid solution.

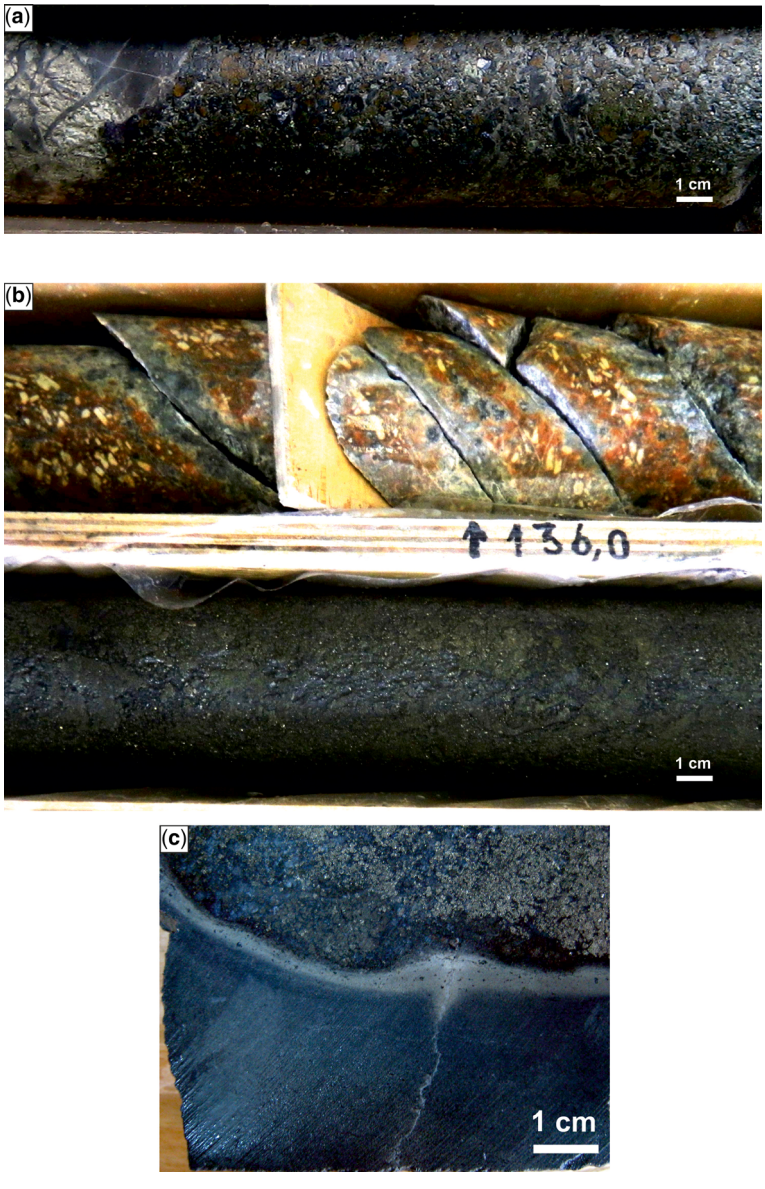

Fig. 11. Late-stage hydrothermal veins and post-mineral andesite dyke: (**a**) hydrothermal Cpy–Gn–Sph pebble vein cutting mineralized and strongly phyllic altered monzonite porphyry; (**b**) hydrothermal Cpy–Py vein cutting mineralized and potassic–phyllic altered monzonite porphyry; and (**c**) xenolith of polymetallic Cpy–Py–Gal–Sph vein enclosed in post-mineral andesite dyke.

solid solution was described in detail by Marushchenko *et al.* (2018). It locally replaces both bornite and chalcopyrite. Native gold (0.001–0.4 mm) forms microinclusions predominantly in bornite and chalcopyrite and locally also in fahlore (Fig. 10c), but rarely in pyrite. The gold fineness ranges from 916 to 954. Pyrite occurs as grains ranging from a few micrometres to a few millimetres in size. It is typically intergrown with chalcopyrite and molybdenite. Fractures within individual pyrite grains are locally filled by fahlore.

Sulfides are also recorded in pebble dykes and hydrothermal breccia dykes that locally intersect the deposit. These dykes consist of angular and

subrounded clasts of altered intrusions and vary in size from millimetres to several centimetres. The clasts are cemented by a matrix of hydrothermal quartz with minor bornite, chalcopyrite and magnetite. Pyrite dominates in the peripheral and upper parts of the hydrothermal system.

Late-stage carbonate–polymetallic mineralization: The late-stage auriferous polymetallic chalcopyrite–pyrite–galena–sphalerite–quartz–calcite veins can be up to 30 cm thick and are recorded cross-cutting the central part of the orebody (preserved xenolith in Fig. 10c). Chalcopyrite of this late-stage phase commonly replaces pyrite and it is intimately intergrown with sphalerite and, less commonly, galena. Additionally, chalcopyrite can form fine-grained disseminations locally arranged along growth zones of host sphalerite and fills fractures in the latter (Fig. 10d–f). Chalcopyrite contains up to 0.02 wt% Zn.

Sphalerite occurs as relatively large individual grains with disseminated chalcopyrite. The mineral has variable Cd content, 0.2–2.0 wt%. Galena grains are variable in size and either fill the interstices between pyrite grains or emplace fractures in sphalerite and/or chalcopyrite grains (Fig. 10f–h). The galena locally contains high Bi, up to 0.6 wt%, but it typically lacks appreciable Ag concentrations. Altaite inclusions are common in galena (Fig. 10i). Fahlore is described in detail by Marushchenko *et al.* (2018), who distinguished five generations: (I, II) tetrahedrite; (III) tennantite locally enriched in Bi; (IV) oscillatory zoned tennantite–tetrahedrite; and (V) goldfieldite and Te-bearing tennantite. The Ag content in the sulfosalts slightly increases from the first to the latest generation (Marushchenko *et al.* 2018).

The precious-metal mineralogy is more complex than in the early-stage porphyry copper–gold–molybdenum assemblage and it includes Au–Ag alloys, petzite, hessite and rare froodite inclusions in hessite. The Au–Ag alloys are represented by two generations. The first one overgrows clausthalite, subsequently being replaced by hessite and petzite within interstices between bornite grains (Fig. 10j) and fractures intersecting the latter. The fineness of this Au–Ag alloy ranges from 815 to 830. The second generation is rare. It fills fractures in gold I (Fig. 10j) and tennatite–tetrahedrite IV (Fig. 10k), and is closely intergrown with hessite (Fig. 10l). Its fineness is 640–750.

The evidence for overprinting high-sulfidation epithermal mineralization is very rare at Peschanka and limited to rare and local paragenesis of chalcopyrite, enargite and Cu-rich tennantite. Native copper is also rare and occurs as small pockets or filling interstices between silicate grains within the least hydrothermal altered monzonite intrusions (Fig. 10m & n).

Economic mineralization is mainly controlled by NE-trending and steeply dipping quartz-sericite zones. The high-grade part (>1.0 wt% Cu) of the orebody directly correlates with the central bornite-rich part of the deposit outlined using a cut-off Cu_{eq} of 0.2 wt% (Fig. 4b). The orebody is steeply dipping towards the east. A narrow, but very high-grade and bornite-rich, ore shoot locally containing up to 8.50 wt% Cu is intersected by several drillholes over a width of about 2 m. We have analysed core samples from 266 drillholes for 40 chemical elements to study empirical relationships between different elements and minerals. The statistical processing of the data obtained revealed three large groups of chemical elements (Fig. 12): (1) Al, Mg, Li, P, Ca, Fe, Co, Ni and Na; (2) K, Cu, Au, Mo, Ag, As, Sb, Bi, Se and and Te; and (3) S, Cd, Pb, Zn and Mn. The siderophile elements of the first group (Fe, Co, Ni), as well as Na, Ca, Al, Mg and Li, are mainly concentrated in the outer pyrite shell or unmineralized propylitic alteration surrounding the stockwork orebodies. Iron, Ni and Co are concentrated in pyrite and possibly magnetite, whereas other are rock-forming elements and are concentrated in metasomatic albite, amphibole, epidote, chlorite and biotite. The elements of the second group illustrate stockwork ore mineralization. Copper is concentrated in copper minerals. Intimate association of gold, silver and copper is explained by that the copper minerals contain Au–Ag alloys as inclusions and fracture filling. Arsenic and Sb are contained in fahlores. Selenium is concentrated in bornite as minor elements or in clausthalite. The presence of potassium in this group indicates the association of metals with phyllic alteration. Another confirmation of this association is consistent distribution of copper grade and phyllic alteration identified in the core from one drillhole (Fig. 13). The third group includes elements composing minerals of the late-stage carbonate–polymetallic mineralization, predominantly sphalerite and galena. They are widely distributed both in the stockwork orebodies and in distal veins and veinlets.

Geophysical footprint of the Peschanka porphyry Cu–Au ± Mo deposit

Peschanka is defined by a distinct ellipsoidal negative magnetic anomaly which overlaps with a significant induced polarization (IP) chargeability anomaly and a low resistivity (Fig. 14a–c). The main stockwork zone containing the high-grade copper and gold mineralization corresponds to this distinct magnetic low anomaly (Figs 5 & 14a) consisting of hematite replacing magnetite owing to phyllic alteration and martitization (cf. Kwan and Müller 2020).

An AMT survey reveals an extensive anomaly with low resistivity that reflects the concealed stockwork orebody at depth and can be traced to a depth

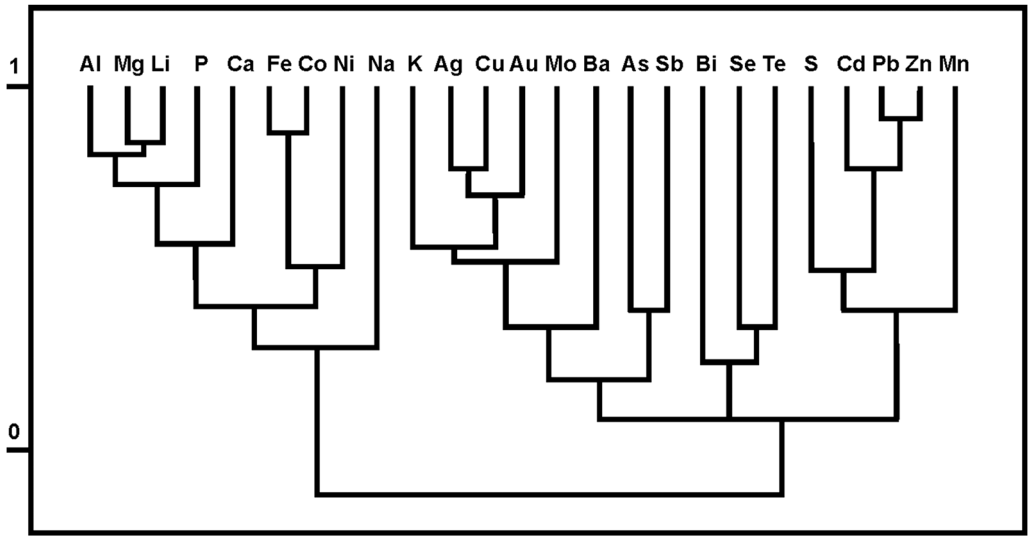

Fig. 12. Correlation dendrogram showing the elemental distribution both in the stockwork ore and in the metasomatic halo at Peschanka.

of >1000 m. These geophysical anomalies suggest that the mineralization vertically extends down to at least 1000 m. The deepest exploration drillholes intersect significant chalcopyrite–bornite–molybdenite mineralization at depths of at least 660 m. During 1975–85 and 2010–13, a series of 184 drillholes totalling 50 764 m were drilled at Peschanka. Another drilling programme is currently in progress (KAZ Minerals 2018).

Structural controls on the Peschanka porphyry Cu–Au ± Mo deposit

Sulfide-bearing veinlets and stringers are synkinematic features and were formed contemporaneously to the stockwork/sheeted vein mineralization at Peschanka. These stringers commonly have lenticular, en-echelon textures and they reflect the extensional displacements along strike-slip, thrust and normal faults (Fig. 15). An integrated structural interpretation of faults and relative displacements along them, as well as their relationships with the orebodies and the distribution and orientation of veins and veinlets at Peschanka are illustrated in Figures 16 and 17 (Chitalin *et al.* 2012).

One of the most important features of Peschanka is the formation of distinct zones with sheeted veining in the orebody reflecting the prevailing stress field during its evolution. This is in contrast to the more 'typical' stockwork orebodies of other porphyry Cu–Au deposits worldwide that usually

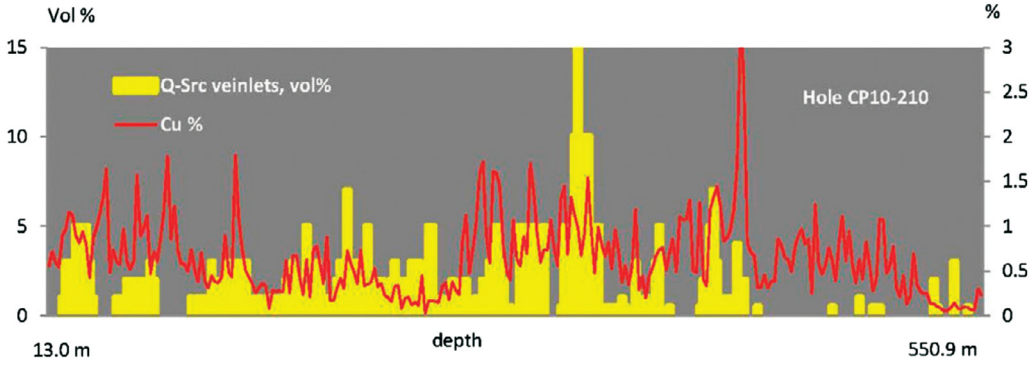

Fig. 13. Plot illustrating variations in copper grade and percentage of quartz–sericite zones.

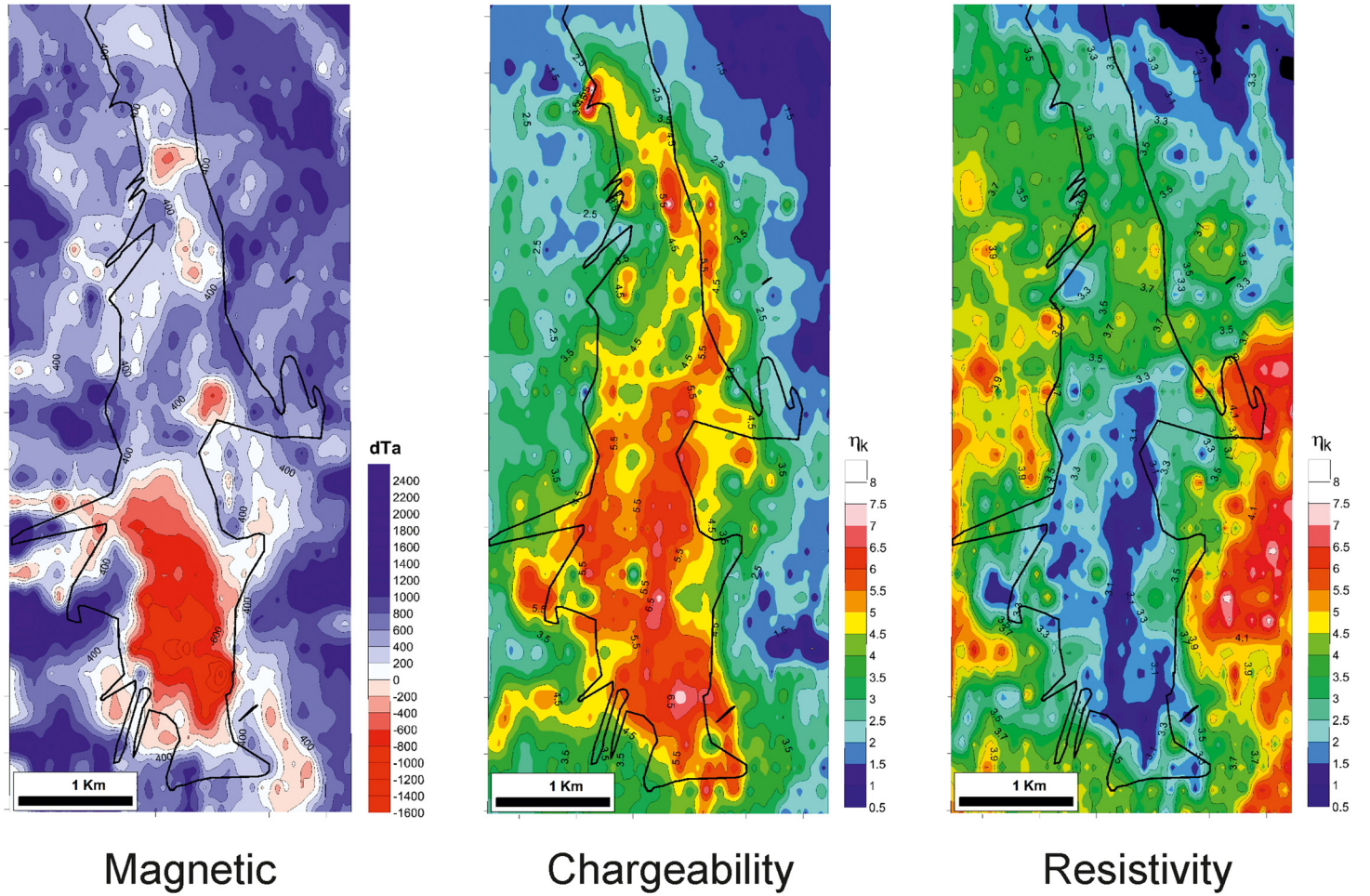

Fig. 14. Geophysical anomalies at the Peschanka deposit (Chitalin *et al.* 2014). Black line outlining the copper mineralization on the surface and at depth. The red colour in the left figure illustrates the magnetic low anomaly.

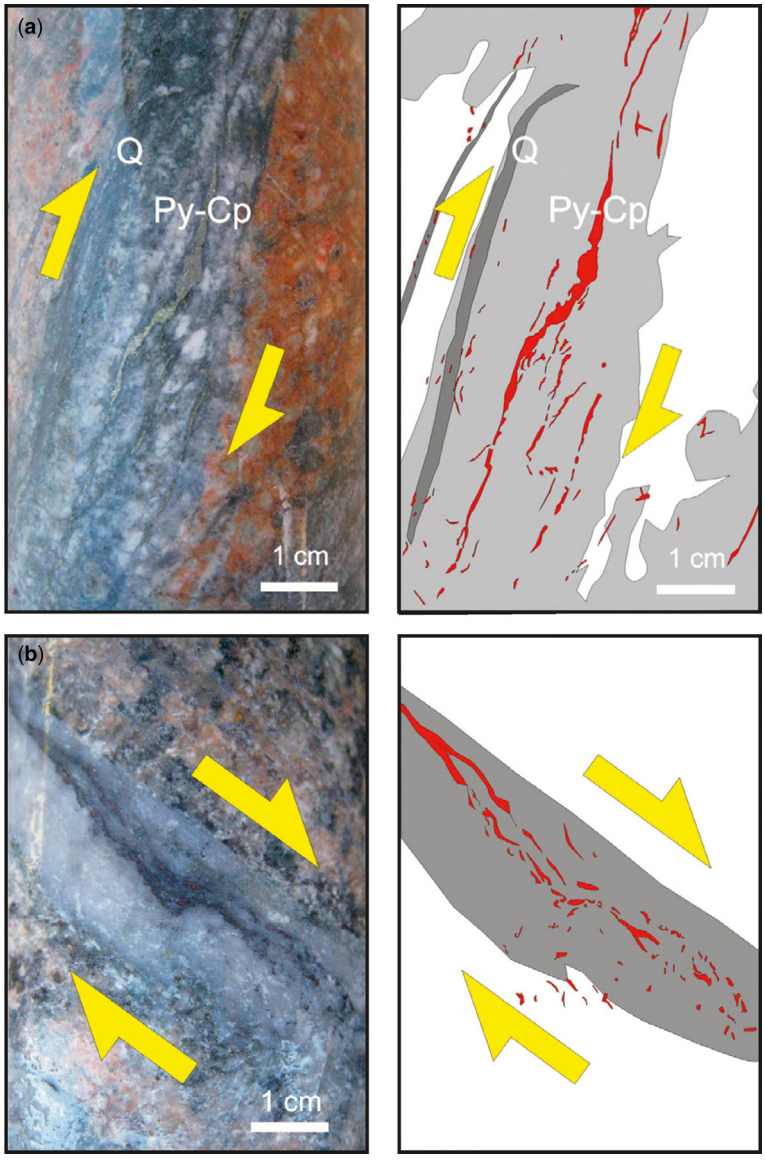

Fig. 15. Syn-kinematic sulfide veinlets documented in drillcore from the Peschanka deposit: (**a**) *en echelon*-type syn-mineral Qtz–Chl–Py ± Cpy vein hosted by phyllic zones that locally overprint the potassic altered monzonite porphyry; (**b**) syn-mineral Bn–Cpy vein cutting early-stage Qtz vein in potassic altered monzodiorite. Note that the top part of this sample represents the hanging wall and the lower part its footwall.

consist of cross-cutting vein generations with multi-directional vein orientations. Figure 18 demonstrates the spatial relationships between high-grade copper mineralization, high-K monzonite intrusions and the stockwork/sheeted vein orebody (Chitalin *et al.* 2012). The high-K igneous intrusions host the quartz–sulfide veining and the related Cu–Au–Mo mineralization. It should be noted that the zones with the most abundant quartz veining represent a low permeability for percolating hydrothermal fluids and, thus, are commonly barren of mineralization (Fig. 19). These highly silicified, but barren, cores are also recorded at several Chilean porphyry Cu ± Mo deposits (e.g. El Salvador). This observation might also explain the spatial discordance between local high-grade ore shoots and zones with abundant

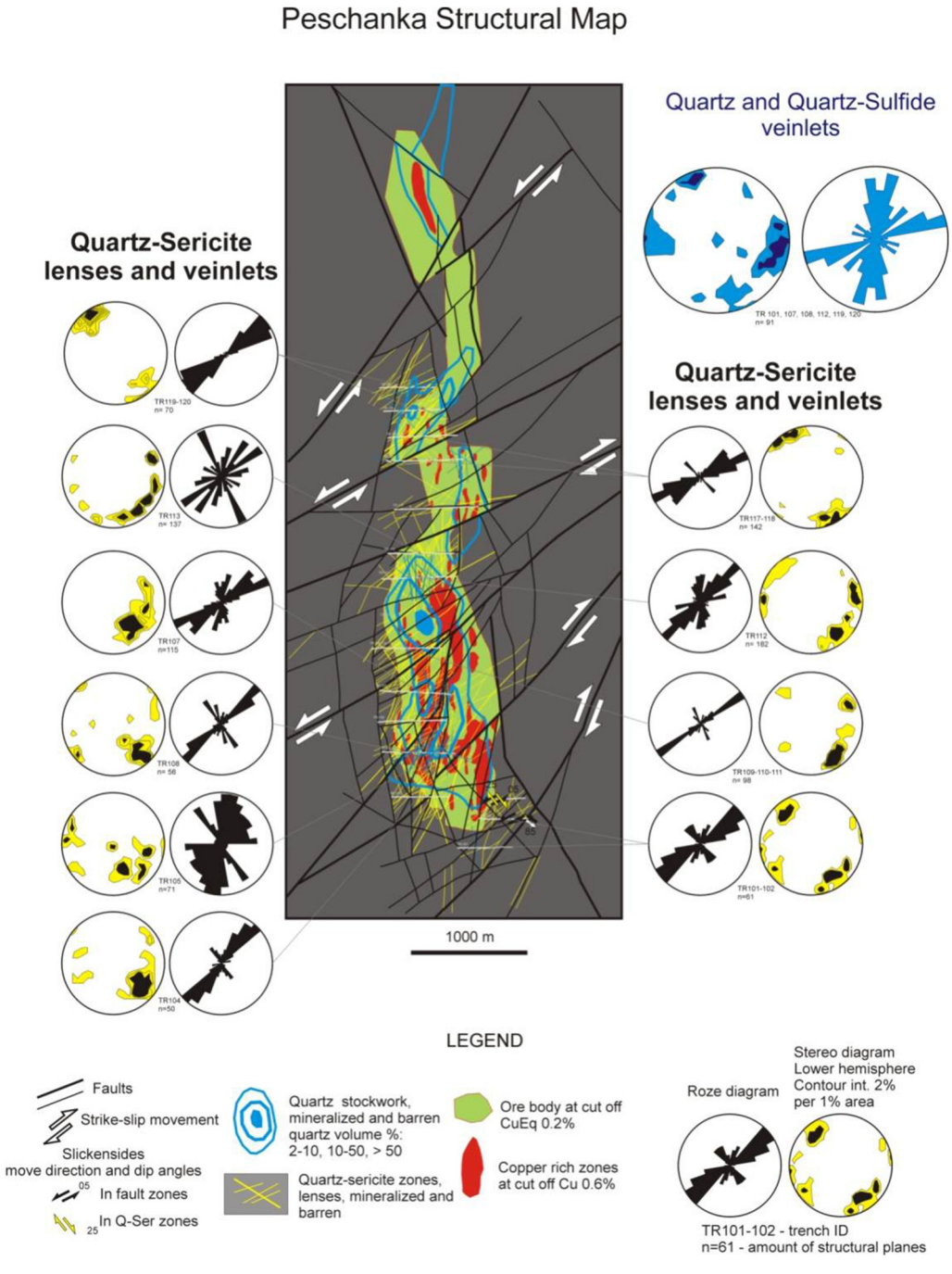

Fig. 16. Integrated structural map of the Peschanka deposit, including rose diagrams and stereograms illustrating the veinlet distributions.

quartz stockwork veining at Peschanka. Based on the proposed strike-slip structural model (Chitalin *et al.* 2012; Fig. 20), the extensional conduits channelling the hydrothermal fluids began to open up contemporaneously with the emplacement of the monzonite stocks.

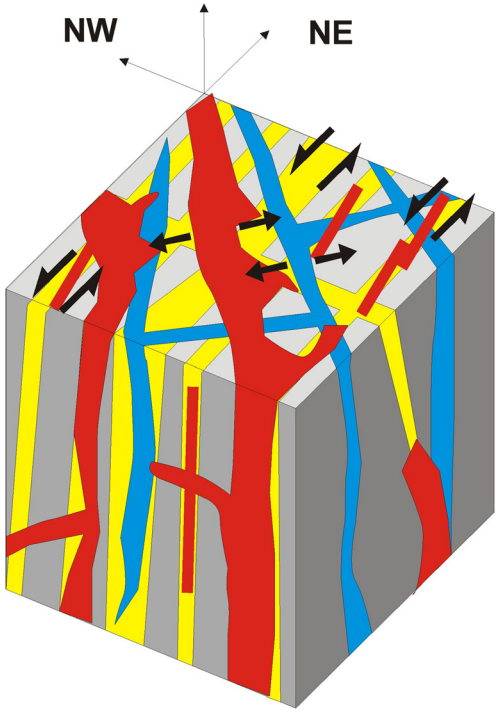

Fig. 17. Conceptual model of the Peschanka vein mineralization: yellow, quartz–sericite altered structures; blue, barren quartz stockwork veins; red, hypogene quartz–sulfide (pyrite, chalcopyrite, bornite, molybdenite) veining; black arrows, kinematic movements.

Whole-rock geochemistry of the Peschanka intrusions

Representative major element compositions of the Peschanka intrusions have been published by Volchkov *et al.* (1982) and Soloviev (2014). The samples are characterized by high K_2O contents (up to 4.57 wt%), high K_2O/Na_2O ratios (0.7–0.9), high Al_2O_3 (>18.1 wt%) and low TiO_2 contents (<0.7 wt%), which are typical for high-K calc-alkaline intrusions (Peccerillo and Taylor 1976; Müller *et al.* 1992). However, the studies by Volchkov *et al.* (1982) and Soloviev (2014) lack trace-element data and our paper is the first study discussing their important role in the genesis of the Peschanka monzodiorites and monzonites. New representative trace-element compositions are presented in Table 1.

The Peschanka intrusions are characterized by high large ion lithophile elements (LILE) such as K_2O, Rb up to 212 ppm, Sr up to 1588 ppm and Ba up to 1997 ppm and elevated light rare earth elements (LREE) such as La and Ce up to 23 and 44 ppm (Table 1). The high LILE and LREE as well as distinctly low high field strength elements, such as TiO_2, Hf up to 2.5 ppm, Y up to 18 ppm and Zr up to 115 ppm reflect the palaeoisland arc setting of Peschanka (cf. Müller *et al.* 1992), as originally proposed by Sidorov and Eremin (1994) and Volkov *et al.* (2006). A palaeosubduction setting is also implied by plotting the samples on the Nb v. Y discrimination diagram (Fig. 21a) by Pearce *et al.* (1984).

The Peschanka intrusions also have high whole-rock La/Yb and Ce/Yb ratios of up to 19 and 37, and high Ta/Yb and Th/Yb ratios of up to 0.46 and 6.41, reflecting their high-K calc-alkaline compositions that are borderline to shoshonites (see also Fig. 21b). The geochemical discrimination diagrams shown in Figure 21b are based on trace elements such as Ta, Th and LREE, which are immobile even during weak hydrothermal alteration (Pearce 1982; Müller *et al.* 1992). Plotting the Peschanka intrusions on the Zr/Ti v. Nb/Yb geochemical discrimination diagram by Winchester and Floyd (1977) also illustrates whole-rock compositions that are borderline to alkaline with the majority of samples falling into the trachyandesite field (Fig. 21c).

Abundant primary magnetite in the Peschanka intrusions, as well as numerous gypsum and anhydrite veins, are suggestive of high oxidation states of the parental magmas (Volkov *et al.* 2006; Chitalin *et al.* 2012). This mineralogical observation is consistent with the high whole-rock Fe_2O_3/FeO ratios of the rocks of 0.8–1.27 (Volchkov *et al.* 1982) and high V/Sc ratios of up to 21.9 (Table 1). Importantly, the whole-rock Eu/Eu* ratios of the Peschanka intrusions are ≥1, which is typical for potassic igneous rocks with high oxidation states (Loader *et al.* 2017). However, three intrusion samples with weak to moderate phyllic alteration have lower Eu/Eu* ratios of ≤0.55 (cf. Table 1), suggesting the mobilization of Eu during the replacement of primary plagioclase phases by hydrothermal sericite. Abundant amphibole and biotite phenocrysts of the high-K intrusions as well as their high whole-rock Sr/Y ratios of up to 225 (averaging 59) reflect the high water contents of their parental melts (Table 1).

Discussion

Ongoing studies on the genesis of porphyry Cu–Au deposits since their original definition in the classic papers by Sillitoe (1972, 1973, 1979), Titley (1972) and Gustavson and Hunt (1975) reveal the important role of the geochemical composition of their parental intrusions (e.g. Müller and Groves 2019, and references therein). Ore deposits associated with high-K igneous rocks tend to be particularly Au-rich (Mavrogenes *et al.* 2006; Li and

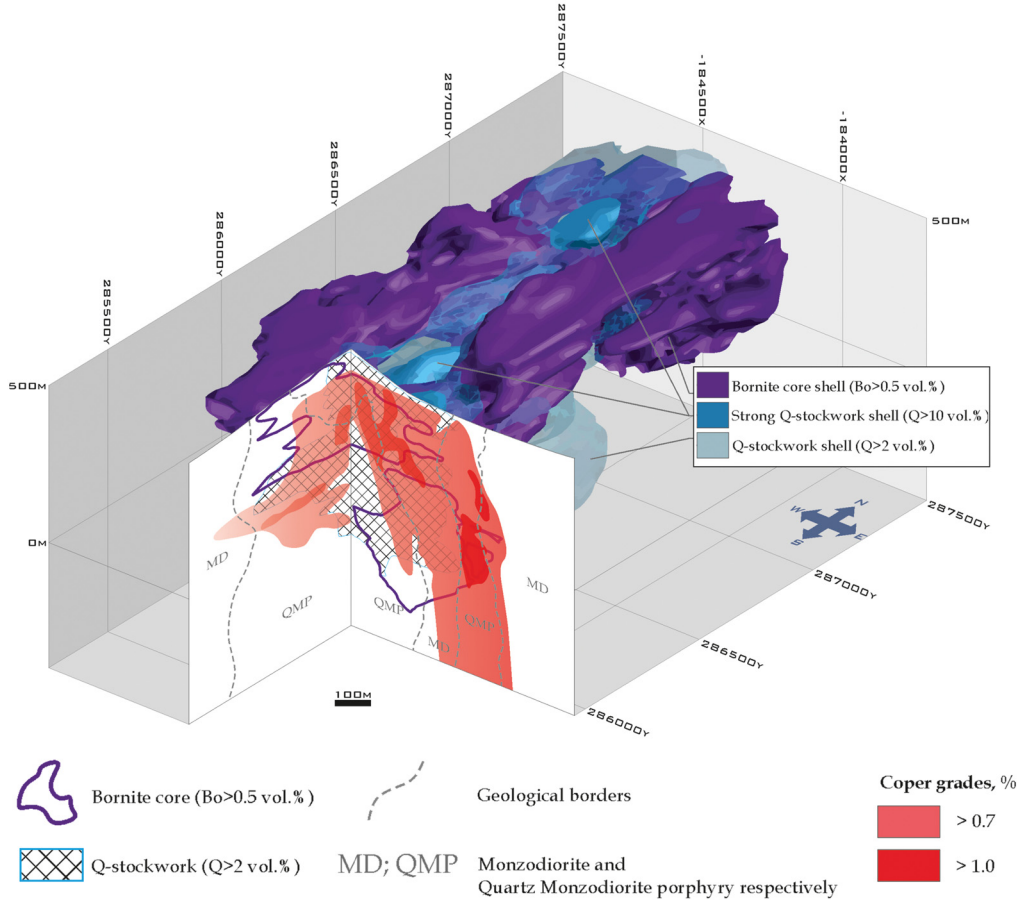

Fig. 18. 3D block model of the Peschanka porphyry Cu–Au–Mo deposit showing the spatial relationships between high-grade mineralization, high-K monzonite intrusions and quartz stockwork/sheeted vein orebody.

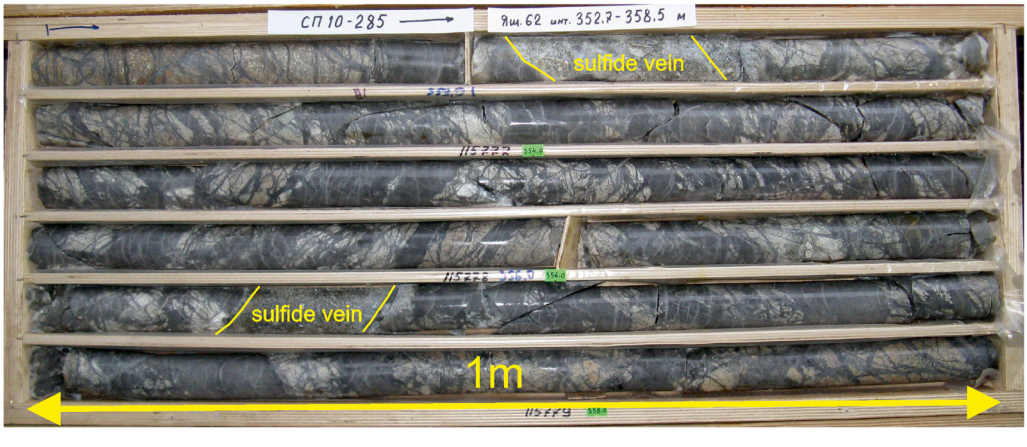

Fig. 19. Intense, but sulfide-free and barren, quartz stockwork veining at the foot-zone of the Peschanka orebody. Rare late-stage sulfide veins cut the quartz stockwork.

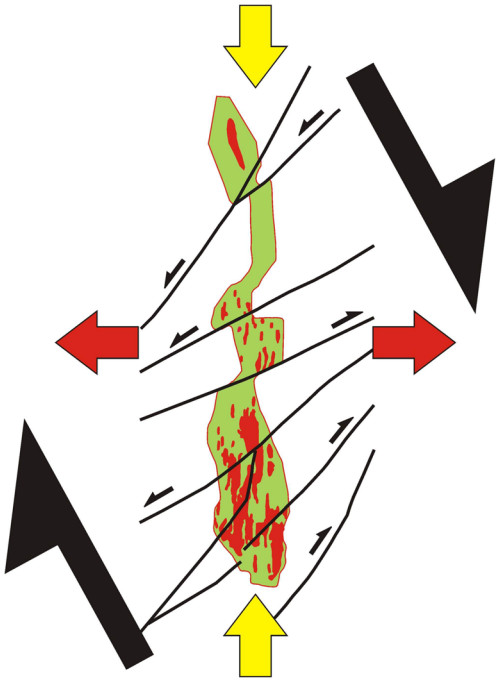

Fig. 20. Structural model of the Peschanka deposit. Extensional sinistral strike-slip structures formed in response to a major regional-scale dextral shear along the Baimka trend. The orebody with a cutoff grade of 0.2 wt% Cu_{eq} is shown in green; high-grade zones at a cutoff of >0.6 wt% Cu are shown in red.

Audetat 2013), probably owing to the high Au solubility in volatile-rich alkali-chloride-bearing fluids (Zajacz *et al.* 2010) and a lack of sulfides in the mantle source region owing to the high oxygen fugacities of these magmas (Mungall 2002; Cocker *et al.* 2016).

The Peschanka porphyry Cu–Au ± Mo deposit is hosted by monzodiorite and monzonite intrusions with distinctly high-K calc-alkaline to shoshonitic compositions, comparable with other major porphyry Cu–Au deposits such as Bingham, Utah (Maughan *et al.* 2002), Grasberg, Indonesia (Pollard *et al.* 2005), Oyu Tolgoi, Mongolia (Crane and Kavalieris 2012) and Pebble, Alaska (Olson *et al.* 2017). The abundant amphibole and biotite phenocrysts of the Peschanka intrusions as well as their high whole-rock Sr/Y ratios of up to 225 (averaging 59) reflect very high H_2O contents of their parental melts. Importantly, modern studies (e.g. Loucks 2014; Olson *et al.* 2017) suggest that high H_2O contents of igneous rocks are also reflected in high whole-rock Sr/Y ratios (>30). In water-rich magmas, the H_2O content increases with fractionation (Cocker *et al.* 2016). During fractional crystallization, Y behaves as a compatible element in hornblende phenocrysts and is depleted from the melt as hornblende and pyroxene accumulate at the bottom of the magma chamber, while Sr is incompatible and remains in the residual melt (Loucks 2014), at least until the onset of plagioclase fractionation.

Recent work confirms that melts and hydrothermal fluids with elevated oxygen fugacities are favourable for Cu solubility (Li *et al.* 2017). High oxidation states in potassic igneous rocks are also suggested by experimental studies (e.g. Li and Audetat 2013). While the f_{O2} of low-K tholeiites (mid-ocean ridge basalt) ranges between −2.0 and +0.7 log units from the fayalite–magnetite–quartz (FMQ) buffer, high-K island arc basalts typically have high f_{O2} ranging from +0.3 to +6.0 log units ΔFMQ (Lee *et al.* 2005). A high f_{O2} of arc magmas is also reflected in the presence of magmatic anhydrite and cross-cutting gypsum–anhydrite veins in the parental intrusions of many large porphyry Cu–Au (e.g. Stern *et al.* 2007; Yang *et al.* 2008) and related epithermal gold deposits (e.g. Müller *et al.* 2002). At constant temperatures, as f_{O2} increases, the concentration of dissolved sulfide (S^{2-}) in the melt decreases, whereas the dissolved sulfate (SO_4^{2-}) increases as sulfur is oxidized (Richards 2011; Zhong *et al.* 2018). Thus, the potential for precious-metal segregation into magmatic sulfide phases is reduced (Zhong *et al.* 2018). At high f_{O2}, sulfate phases have a much higher solubility in silicate melts than sulfides (Ballard *et al.* 2002). If the sulfide concentration in the melt is reduced, gold and copper will be concentrated in the volatile-enriched top part of the magma chamber (Müller *et al.* 2002). Once volatile saturation occurs, the magma chamber releases pulses of metal- and volatile-enriched melts capable of forming porphyry Cu–Au mineralization in the upper crust (Richards 2011).

Although structural controls on the location of porphyry Cu–Au deposits were underestimated in the classic papers on porphyry systems (e.g. Sillitoe 1972, 1973), modern studies reveal their importance in mineral exploration (e.g. Hou *et al.* 2003; Niemeyer and Munizaga 2008; Amirihanza *et al.* 2018; Zheng *et al.* 2020). The genesis of the Peschanka porphyry Cu–Au deposit is clearly structurally controlled. The prevailing stress field during the evolution of Peschanka in a major regional-scale dextral shear zone has led to the formation of extensional and sinistral strike-slip structures controlling distinct zones with sheeted quartz–bornite veining. The sheeted veining orebodies are defined by unusually high vein densities and high Cu–Au grades. This is in contrast to the more typical stockwork orebodies of other porphyry Cu–Au deposits worldwide that usually consist of cross-cutting vein generations with random multidirectional vein orientations (e.g. Gustavson and Hunt 1975; Pacey *et al.* 2019). Similar to other porphyry Cu–Au deposits worldwide,

Table 1. *Trace element concentrations (ppm) of representative igneous rocks from the Peschanka porphyry Cu–Au ± Mo deposit*

	Sample-ID												
	8904-753-2	SP10-215-171.9	8841-754-7	8552-755-8	SP10-225-355.1	SP10-204-231.3	8842-759-2	SP-10-255-447.9	SP10-221-126	SP10-207-53	SP10-201-42	SP10-227-36.2	SP10-207-208
Rb	22.48	139.22	53.99	25.17	212.66	60.81	78.17	184.26	45.51	69.30	66.42	111.56	15.72
Cs	2.20	2.57	8.42	1.95	3.21	3.92	3.94	2.69	2.99	1.40	3.76	0.87	1.31
Ba	247.10	803.58	625.03	228.35	1997.28	841.91	1333.60	1204.86	1009.64	1056.27	1275.53	860.49	448.47
Pb	44.90	10.55	7.83	9.62	26.70	12.42	11.23	550.67	130.27	22.48	33.80	13.10	23.24
Sr	789.60	651.82	1030.67	741.99	1588.15	744.17	977.82	62.61	876.59	535.84	343.37	323.26	835.26
Th	4.76	4.52	3.65	2.23	3.01	5.05	4.25	7.51	3.54	6.61	2.67	13.47	9.88
U	5.82	3.54	1.57	1.07	4.50	3.85	6.67	8.74	3.74	3.98	1.36	3.26	4.36
Ce	36.82	38.15	44.96	27.90	20.02	32.20	40.17	14.40	29.85	72.94	24.37	44.97	46.42
Pb	44.90	10.55	7.83	9.62	26.70	12.42	11.23	550.67	130.27	22.48	33.80	13.10	23.24
Zr	115.94	72.30	65.82	109.19	67.71	91.45	68.47	67.98	59.31	97.03	58.28	134.56	79.85
Hf	7.09	2.16	2.14	2.53	1.37	1.88	1.48	1.60	1.38	3.15	1.94	4.24	2.32
Ti	4150.63	2683.54	2643.72	4507.02	1725.36	2912.27	3456.14	2235.68	n.a.	n.a.	n.a.	n.a.	n.a.
Nb	17.11	17.13	12.20	9.37	10.61	16.39	18.86	16.19	5.07	13.32	4.79	11.81	10.96
La	14.74	19.21	23.25	13.21	10.36	15.72	20.22	7.04	15.70	32.02	13.96	22.98	21.86
Ce	36.82	38.15	44.96	27.90	20.02	32.20	40.17	14.40	29.85	72.94	24.37	44.97	46.42
Pr	4.99	4.63	5.35	3.67	2.42	4.02	5.09	1.80	3.58	9.52	2.83	5.36	5.93
Nd	20.13	18.03	20.80	15.70	9.22	16.03	20.24	7.19	13.78	41.90	10.63	19.98	24.60
Sm	4.31	3.55	3.87	3.50	1.73	3.27	4.06	1.69	2.65	8.97	2.06	3.99	5.24
Eu	1.11	1.06	1.27	1.12	0.83	1.06	1.41	0.80	0.97	1.35	0.78	0.73	1.27
Gd	4.26	3.73	4.25	3.92	1.95	3.61	4.44	1.94	2.45	8.57	2.09	3.89	5.03
Tb	0.63	0.51	0.52	0.60	0.25	0.50	0.58	0.32	0.33	1.24	0.29	0.54	0.76
Dy	3.32	2.65	2.60	3.33	1.34	2.83	3.13	1.98	1.75	6.88	1.59	3.15	4.15
Ho	0.62	0.44	0.43	0.60	0.24	0.49	0.52	0.37	0.31	1.25	0.29	0.59	0.81
Er	1.91	1.31	1.35	1.80	0.76	1.49	1.61	1.18	1.02	3.75	0.97	1.93	2.54
Tm	0.26	0.17	0.17	0.24	0.11	0.20	0.21	0.16	0.15	0.51	0.14	0.30	0.45
Yb	1.85	1.10	1.19	1.55	0.81	1.39	1.43	1.17	1.02	3.38	1.13	2.23	2.59
Lu	0.28	0.15	0.17	0.22	0.13	0.21	0.21	0.17	0.17	0.51	0.18	0.32	0.38
Y	16.840	13.119	12.661	17.910	7.038	14.676	15.790	12.561	8.87	32.53	8.47	16.60	20.78
W	3.44	13.65	1.19	3.53	16.15	5.14	2.20	36.30	3.84	1.12	2.25	1.97	2.69
Tl	0.13	0.65	0.34	0.28	1.49	0.28	0.35	1.36	0.41	0.44	0.54	0.76	0.13
Bi	0.98	0.45	0.02	b.d.l.	1.13	0.31	b.d.l.	0.25	0.02	0.28	0.36	0.29	0.10
P	1756.36	1500.79	1828.51	2117.16	795.18	1954.13	2329.66	2245.51	n.a.	n.a.	n.a.	n.a.	n.a.

Sc	8.27	7.92	8.90	26.07	4.13	6.76	11.03	11.20	n.a.	n.a.	n.a.	n.a.	n.a.
V	181.25	120.28	106.00	204.22	86.93	135.05	139.60	172.98	84.91	361.64	81.52	28.55	139.77
Cr	39.71	107.12	18.00	472.14	107.32	134.13	230.07	63.11	26.62	27.03	69.33	2.29	8.41
Co	6.38	4.00	11.44	27.62	3.50	8.25	12.96	1.99	7.84	23.59	5.79	1.21	7.20
Ni	3.18	b.d.l.	2.80	198.06	b.d.l.	2.03	8.23	b.d.l.	23.15	11.16	29.95	2.02	4.51
Cu	349.57	5627.33	195.04	63.13	10031.57	1561.45	275.48	4388.44	657.57	174.97	1499.40	3643.02	67.43
Zn	231.62	19.61	51.60	96.38	124.85	84.26	103.01	813.32	285.14	105.92	145.71	55.75	70.98
Ga	23.47	20.92	20.41	18.35	20.99	21.86	20.15	25.98	19.55	20.33	18.86	15.70	19.26
Li	21.00	20.02	30.73	62.51	5.18	15.61	18.43	19.15	14.96	2.06	11.45	0.00	25.65
Be	2.36	1.55	2.38	1.72	1.74	2.56	2.43	1.52	n.a.	n.a.	n.a.	n.a.	n.a.
Mo	4.53	15.44	2.28	1.69	16.17	9.69	3.76	125.95	63.15	4.37	2.94	21.89	4.90
Cd	0.51	0.07	0.07	0.14	0.83	0.11	0.05	2.08	0.83	0.12	0.59	0.19	0.08
Mn	n.a.	n.a.	n.a.	n.a.	n.a.	n.a.	n.a.	n.a.	1537.86	2860.08	668.03	172.92	847.03
Ta	n.a.	n.a.	n.a.	n.a.	n.a.	n.a.	n.a.	n.a.	0.10	0.61	0.17	1.03	0.62
Ag	n.a.	n.a.	n.a.	n.a.	n.a.	n.a.	n.a.	n.a.	0.97	0.94	0.88	2.00	0.52
Sn	n.a.	n.a.	n.a.	n.a.	n.a.	n.a.	n.a.	n.a.	1.27	2.46	0.86	1.60	4.18
Sb	0.62	0.36	0.08	0.38	0.69	0.35	0.59	0.91	0.40	3.83	0.41	0.82	0.99
Eu/Eu*	1.14	0.97	1.08	0.99	0.49	0.91	1.13	0.48	0.68	2.33	0.55	1.05	1.36
Th/Nb	0.28	0.26	0.30	0.24	0.28	0.31	0.23	0.46	0.70	0.50	0.56	1.14	0.90
Sr/Y	46.89	49.69	81.40	41.43	225.66	50.70	61.93	4.98	98.82	16.47	40.53	19.47	40.19
La/Yb	7.97	17.49	19.49	8.52	12.76	11.32	14.11	6.01	15.40	9.47	12.40	10.29	8.45
Nb/Y	1.02	1.31	0.96	0.52	1.51	1.12	1.19	1.29	0.57	0.41	0.57	0.71	0.53
Ce/Yb	19.92	34.73	37.68	18.01	24.65	23.17	28.04	12.30	29.27	21.58	21.65	20.13	17.95
Th/Yb	2.57	4.11	3.06	1.44	3.71	3.63	2.97	6.41	3.47	1.96	2.37	6.03	3.82
Ta/Yb									0.10	0.18	0.15	0.46	0.24
Zr/Ti	0.03	0.03	0.02	0.02	0.04	0.03	0.02	0.03					
V/Sc	21.91	15.18	11.91	7.83	21.04	19.98	12.65	15.44					

8904-753-2, Propylitic altered monzodiorite; SP10-215-171.9, potassic altered monzodiorite; 8841-754-7, weakly altered monzonite; 8552-755-8, andesite tuff; SP10-225-355.1, phyllic altered monzodiorite; SP10-204-231.3, potassic altered monzodiorite; 8842-759-2, propylitic altered monzonite; SP-10-255-447.9, phyllic altered monzodiorite; SP10-221-126, fresh monzonite porphyry with large potassic feldspar phenocrysts; SP10-207-53, weakly altered monzodiorite; SP10-201-42, weakly altered monzonite porphyry; SP10-227-36.2, fresh quartz–syenite porphyry; SP10-207-208, weakly phyllic altered monzodiorite with minor sulfide mineralization. n.a., Element not analysed; b.d.l., below detection limit.

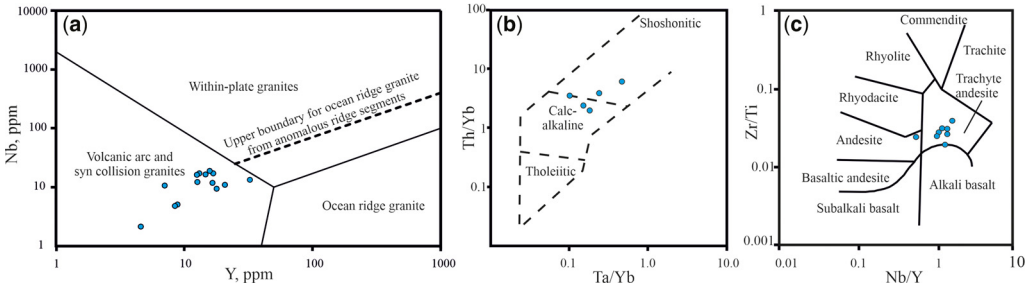

Fig. 21. Binary diagrams illustrating the geochemical fingerprints of the Peschanka intrusions: (**a**) Nb v. Y discrimination diagram after Pearce *et al.* (1984) indicating the arc-related features of the intrusions; (**b**) Th/Yb v. Ta/Yb diagram of Pearce (1982) showing the high-K calc-alkaline to shoshonitic compositions of the intrusions; and (**c**) the Zr/Ti v. Nb/Y discrimination diagram of Winchester and Floyd (1977) illustrating their compositions that are borderline to alkaline with the majority of samples plotting in the trachyandesite field.

Peschanka is also defined by a distinct hydrothermal alteration zonation. However, the lack of advanced argillic alteration assemblages is another distinct feature of the Peschanka porphyry Cu–Au ± Mo deposit.

Conclusions

The Cretaceous Peschanka porphyry Cu–Au ± Mo deposit contains a resource of >9.5 Mt of copper at an average grade of 0.43 wt% and 16.5 Moz of gold at a high average grade of 0.23 g/t, ranking it among the top 10 undeveloped greenfield copper projects worldwide.

Porphyry Cu–Au ± Mo mineralization is hosted by monzodiorite and monzonite intrusions with high-K calc-alkaline to shoshonitic compositions, which are dated at 144.1 ± 1.5 Ma using U/Pb zircon methods. Peschanka is defined by distinct hydrothermal alteration zones including potassic, phyllic, propylitic and argillic assemblages, but a distinct lack of advanced argillic alteration. Late-stage polymetallic assemblages overprint the main Cu–Au ± Mo stockwork zone.

The Peschanka intrusions are intersected by abundant cross-cutting gypsum and anhydrite veins that are suggestive of the high oxidation states of their parental magmas. This mineralogical interpretation is consistent with the high whole-rock Fe_2O_3/FeO ratios and high V/Sc ratios of the rocks of up to 1.27 and up to 21.9, respectively. The whole-rock Eu/Eu* ratios of the Peschanka intrusions are ≥1 which is also typical for high-K igneous rocks with high oxidation states. Abundant amphibole and biotite phenocrysts of the high-K intrusions as well as their high whole-rock Sr/Y ratios of up to 225 (avg. 59) reflect the high H_2O contents of the parental melts.

Hypogene vein-hosted and disseminated Cu–Au ± Mo sulfide mineralization at Peschanka are structurally controlled by significant NE-trending strike-slip faults that acted as the conduits for the hydrothermal fluids. The central part of the orebody consists of high-grade subvertical and north–south-trending sheeted quartz–bornite veining with unusually high vein densities. Economic Cu and Au grades are directly correlated with high vein densities.

Acknowledgements We are very grateful to the constructive reviews by two anonymous reviewers and the editors Chalapathi Rao and Lukáš Krmíček which have greatly improved the manuscript.

Author contributions **AFC**: writing – original draft (lead); **IAB**: writing – original draft (equal); **YNN**: writing – original draft (equal); **GTD**: writing – original draft (equal); **YNK**: writing – original draft (equal); **DM**: writing – original draft (equal)

Funding The results of the section 'Whole-rock geochemistry of the Peschanka intrusions' were obtained within the Russian Science Foundation grant (project no. 19-17-00200).

Data availability All data generated or analysed during this study are included in this published article.

Appendix

The electron microscope study was performed using a Jeol JSM_6480LV scanning_electron microscope equipped with an INCA Wave_500 WDS and INCA Energy_350 EDS at the Laboratory of local methods of matter investigation at the Department of Geology (MSU). The BSE images were obtained using an accelerating voltage of 20 kV and a current of ~2 nA. The mineral compositions were determined using energy-dispersive spectrometry at an accelerating voltage of 20 kV and a current of 2 nA for silicate minerals and 0.7 nA for sulfides and native gold.

References

Akinin, V.V. and Miller, E.L. 2011. Evolution of calc-alkaline magmas of the Okhotsk-Chukotka volcanic belt. *Petrology*, **19**, 237–277, https://doi.org/10.1134/S0869591111020020

Amirihanza, H., Shafieibafti, S., Derakhshani, R. and Khojastehfar, S. 2018. Controls on Cu mineralization in central part of the Kerman porphyry copper belt, SE Iran: constraints from structural and spatial pattern analysis. *Journal of Structural Geology*, **116**, 159–177, https://doi.org/10.1016/j.jsg.2018.08.010

Baksheev, I.A., Prokof'ev, V.Yu. *et al*. 2012. Tourmaline as a prospecting guide for the porphyry-style deposits. *European Journal of Mineralogy*, **24**, 957–979, https://doi.org/10.1127/0935-1221/2012/0024-2241

Ballard, J.R., Palin, J.M. and Campbell, I.H. 2002. Relative oxidation states of magmas inferred from Ce (IV)/Ce (III) in zircon: application to porphyry copper deposits of northern Chile. *Contributions to Mineralogy and Petrology*, **144**, 347–364, https://doi.org/10.1007/s00410-002-0402-5

Bouse, R.M., Ruiz, J., Titley, S.R., Tosdal, R.M. and Wooden, J.L. 1999. Lead isotope compositions of Late Cretaceous and early Tertiary igneous rocks and sulfide minerals in Arizona; implications for the sources of plutons and metals in porphyry copper deposits. *Economic Geology*, **94**, 211–244, https://doi.org/10.2113/gsecongeo.94.2.211

Chitalin, A.F. 2019. Structural paragenesis and ore mineralization of the Baimskaya shear zone, Western Chukotka. Russian tectonophysics. *On the Occasion of the 100th Anniversary of M.V. Gzovsky*. RIO KSC RAS, Apatity, 333–349 [in Russian].

Chitalin, A., Fomichev, E., Usenko, V., Agapitov, D. and Shtengelov, A. 2012. Structural model of Peschanka porphyry Cu–Au–Mo deposit, Western Chukotka, Russia *Structural Geology and Resources – 2012. Bulletin no. 56-2012. Symposia*, 26–28 September 2012, Kalgoorlie, Western Australia.

Chitalin, A.F., Usenko, V.V., Fomichev, E.V. 2013. Baimka ore zone – cluster of large, deposits of nonferrous and precious metals at the East of Chukotka // Mineral resourses of Russia. *Economics & Management: Scientific and Technical Journal*, **2013**, 68–73 [in Russian].

Chitalin, A.F., Nikolaev, Yu.N. *et al*. 2014. *Exploration work in Baimka licensed area*. Unpublished report [in Russian].

Chitalin, A.F., Nikolaev, Yu.N. *et al*. 2016. Porphyry–epithermal systems of the Baimka Ore Zone, Western Chukotka. *Smirnovskiy sbornik – 2016*, Moscow, 82–115. http://www.geol.msu.ru/news/smirnov_2016.pdf [in Russian]

Cocker, H.A., Valente, D.L., Park, J.W. and Campbell, I.H. 2016. Using platinum group elements to identify sulfide saturation in a porphyry Cu system: the El Abra porphyry Cu deposits, northern Chile. *Journal of Petrology*, **56**, 2491–2514, https://doi.org/10.1093/petrology/egv076

Crane, D. and Kavalieris, I. 2012. Geologic overview of the Oyu Tolgoi porphyry Cu–Au–Mo deposits, Mongolia. *Economic Geology Special Publications*, **16**, 187–213, https://doi.org/10.5382/SP.16.09

Gustavson, L.B. and Hunt, J.P. 1975. The porphyry copper deposit at El Salvador, Chile. *Economic Geology*, **70**, 857–912, https://doi.org/10.2113/gsecongeo.70.5.857

Hou, Z.Q., Ma, H. *et al*. 2003. The Himalayan Yulong Porphyry Copper Belt: product of large-scale strike-slip faulting in Eastern Tibet. *Economic Geology*, **98**, 125–145, https://doi.org/10.2113/gsecongeo.98.1.125

Kara, T.V., Tikhomirov, P.L. and Demin, A.D. 2019. New data on the age of magmatic events in the Oloy fold zone, Western Chukotka: evidence from U–Pb zircon dating. *Doklady Earth Sciences*, **489**, 911–916, https://doi.org/10.1134/S1028334X19080269

KAZ Minerals. 2018. Kaz Minerals press release 2018: https://www.kazminerals.com/repository/news-container/news/2018/kaz-minerals-acquires-baimskaya-copper-project

Kondratiev, M.N., Savva, N.E., Gamyanin, G.N., Kolova, E.E., Semyshev, F.I., Malinovsky, M.A. and Kondratieva, E.A. 2017. New data on the structure, mineralogy, and geochemistry of Karalveem gold deposit (Chukotka). *Otechestvennaya Geologiya*, **3**, 23–44 (in Russian).

Kwan, K. and Müller, D. 2020. Mount Milligan alkalic porphyry Au–Cu deposit, British Columbia, Canada, and its AEM and AIP signatures: implications for mineral exploration in covered terrains. *Journal for Applied Geophysics*, **180** (in press), https://doi.org/10.1016/j.jappgeo.2020.104131

Lee, C.T.A., Leeman, W.P., Canil, D. and Li, Z.X.A. 2005. Similar V/Sc systematic in MORB and arc basalts: implications for the oxygen fugacities of their mantle source regions. *Journal of Petrology*, **46**, 2313–2336, https://doi.org/10.1093/petrology/egi056

Li, Y. and Audetat, A. 2013. Gold solubility and partitioning between sulfide liquid, monosulfide solid solution and hydrous mantle melts: implications for the formationof Au-rich magmas and crust-mantle differentiation. *Geochimica et Cosmochimica Acta*, **118**, 247–262, https://doi.org/10.1016/j.gca.2013.05.014

Li, Y., Selby, D., Feely, M., Costanzo, A. and Li, X.H. 2017. Fluid inclusion characteristics and molybdenite Re–Os geochronology of the Qulong porphyry coppermolybdenum deposit Tibet. *Mineralium Deposita*, **52**, 137–158, https://doi.org/10.1007/s00126-016-0654-z

Loader, M.A., Wilkinson, J.J. and Armstrong, R.N. 2017. The effect of titanite crystallisation on Eu and Ce anomalies in zircon and its implications for the assessment of porphyry Cu deposit fertility. *Earth Planetary Science Letters*, **472**, 107–119 https://doi.org/10.1016/j.epsl.2017.05.010

Loucks, R.R. 2014. Distinctive composition of copper-ore forming arc magmas. *Australian Journal of Earth Sciences*, **61**, 5–16, https://doi.org/10.1080/08120099.2013.865676

Marushchenko, L.I. 2013. The mineralogy of propylites of the large Peschanka porphyry copper deposit (West Chukotka). *Moscow University Geology Bulletin*, **68**, 79–88, https://doi.org/10.3103/S0145875213020075

Marushchenko, L.I., Baksheev, I.A., Nagornaya, E.V., Chitalin, A.F., Nikolaev, Yu.N., Kalko, I.A. and Prokofiev, V.Yu. 2015. Quartz–sericite and argillic alterations at the Peschanka Cu–Mo–Au deposit, Chukchi Peninsula,

Russia. *Geology of Ore Deposits*, **57**, 213–225, https://doi.org/10.1134/S1075701515030034

Marushchenko, L.I., Baksheev, I.A., Nagornaya, E.V., Chitalin, A.F., Nikolaev, Yu.N and Vlasov, E.A. 2018. Compositional evolution of the tetrahedrite solid solution in porphyry-epithermal system: a case study of the Baimka Cu–Mo–Au trend, Chukchi Peninsula, Russia. *Ore Geology Reviews*, **103**, 21–37, https://doi.org/10.1016/j.oregeorev.2017.01.018

Maughan, D.T., Keith, J.D., Christiansen, E.H., Pulsipher, T., Hattori, K. and Evans, N.J. 2002. Contributions from mafic alkaline magmas to the Bingham porphyry Cu–Au–Mo deposit, Utah, USA. *Mineral Deposita*, **37**, 14–37, https://doi.org/10.1007/s00126-001-0228-5

Mavrogenes, J.A., Scaillet, B., Pichavant, M. and England, R.N. 2006. The connection between high-K melts and Au deposits: evidence from natural and experimental systems. *Geochimica et Cosmochimica Acta*, **70**, A404, https://doi.org/10.1016/j.gca.2006.06.815

Migachev, I.F., Girphanov, M.M. and Shishakov, V.B. 1985. Porphyry copper Peschanka deposit. *Rudy i Metally*, **3**, 48–68 [in Russian].

Moll-Stalcup, E.J., Lane, L.S., Cecile, M.P. and Gorodinsky, M.E. 1995. Geochemistry and U–Pb geochronology of arc-related magmatic rocks, Northeastern Russia. *Abstracts of the Geological Society of America, 91st Anniversary, Cordilleran Section*, Columbus, Ohio, **27**, 65.

Müller, D. 2002. Preface – gold-copper mineralization in alkaline rocks. *Mineralium Deposita*, **37**, 1–3, https://doi.org/10.1007/s00126-001-0226-7

Müller, D. and Groves, D.I. 1993. Direct and indirect association between potassic igneous rocks, shoshonites, and gold–copper deposits. *Ore Geology Reviews*, **8**, 383–406, https://doi.org/10.1016/0169-1368(93)90035-W

Müller, D. and Groves, D.I. 2019. *Potassic Igneous Rocks and Associated Gold–Copper Mineralization*. 5th edn. Mineral Resource Reviews, Springer Nature, Cham, Switzerland.

Müller, D., Rock, N.M.S. and Groves, D.I. 1992. Geochemical discrimination between shoshonitic and potassic volcanic rocks from different tectonic settings: a pilot study. *Mineralogy and Petrology*, **46**, 259–289, https://doi.org/10.1007/BF01173568

Müller, D., Heithersay, P.S. and Groves, D.I. 1994. The shoshonite porphyry Cu–Au association in the Goonumbla district, N.S.W., Australia. *Mineralogy and Petrology*, **51**, 299–321, https://doi.org/10.1007/BF01159734

Müller, D., Herzig, P.M., Scholten, J.C., Hunt, S. 2002. Ladolam gold deposit, Lihir Island, Papua New Guinea: gold mineralization hosted by alkaline rocks. *Economic Geology Special Publication*, **9**, 367–382.

Mungall, J.E. 2002. Roasting the mantle: slab melting and the genesis of major Au and Au-rich Cu deposits. *Geology*, **30**, 915–918, https://doi.org/10.1130/0091-7613(2002)030<0915:RTMSMA>2.0.CO;2

Mutschler, F.E. and Mooney, T.C. 1993. Precious metal deposits related to alkaline igneous rocks – provisional classification, grade-tonnage data, and exploration frontiers. *In*: Kirkham, R.V., Sinclair, W.D., Thorpe, R.I. and Duke, G.M. (eds) *Mineral Deposits Modeling*. Geological Association of Canada, Special Papers, **40**.

Nagornaya, E.V., Baksheev, I.A., Selby, D. and Tikhomirov, P.L. 2020. The latest Aptian/earliest Albian age of the Kekura gold deposit, Western Chukotka, Russia: implications for mineralization associated with post-collisional magmatism. *Mineralium Deposita*, **55**, 1255–1262, https://doi.org/10.1007/s00126-020-00969-7

Niemeyer, H. and Munizaga, R. 2008. Structural control of the emplacement of the Portrerillos porphyry copper, central Andes of Chile. *Journal of South American Earth Sciences*, **26**, 261–270, https://doi.org/10.1016/j.jsames.2008.08.006

Nikolaev, Yu.N., Kalko, I.A. *et al*. 2020. The Oloy zone: gold–silver mineralization and its economic prospects. *Otechesnvennya Gerologiya*, **1**, 66–79, https://doi.org/10.24411/0869-7175-2020-10005

Nokleberg, W.J., Parfenov, L.M. *et al*. 2001. Phanerozoic tectonic evolution of the Circum-North Pacific. *US Geological Survey, Professional Papers*, 1626, http://geopubs.wr.usgs.gov/profpaper/pp1626/

Olson, N., Dilles, J.H., Kent, A.J.R. and Lang, J.R. 2017. Geochemistry of the Cretaceous Kaskanak batholith and genesis of the pebble porphyry Cu–Au–Mo deposit, southwest Alaska. *American Mineralogist*, **102**, 1597–1621, https://doi.org/10.2138/am-2017-6053

Pacey, A., Wilkinson, J., Owens, J., Priest, D., Cooke, D.R. and Millar, I.L. 2019. The anatomy of an alkalic porphyry Cu–Au system: geology and alteration at Northparkes Mines, NSW, Australia. *Economic Geology*, **114**, 441–472, https://doi.org/10.5382/econgeo.4644

Parfenov, L.M. 1991. Tectonics of the Verkhoyansk–Kolyma Mesozoides in the context of plate tectonics. *Tectonophysics*, **199**, 319–342, https://doi.org/10.1016/0040-1951(91)90177-T

Parfenov, L.M., Badarch, G. *et al*. 2009. Summary of Northeast Asia geodynamics and tectonics. *Stephan Mueller Special Publications*, **4**, 11–33, https://doi.org/10.5194/smsps-4-11-2009

Pearce, J.A. 1982. Trace element characteristics of lavas from destructive plate boundaries. *In*: Thorpe, R.S. (ed.) *Andesites*. Wiley, New York, 525–548.

Pearce, J.A., Harris, N.B.W. and Tindle, A.G. 1984. Trace element discrimination diagrams for the tectonic interpretation of granitic rocks. *Journal of Petrology*, **24**, 956–983, https://doi.org/10.1093/petrology/25.4.956

Peccerillo, A and Taylor, S.R. 1976. Geochemistry of Eocene calc-alkaline volcanic rocks from the Kastamonon area, northern Turkey. *Contributions to Mineralogy and Petrology*, **58**, 63–81, https://doi.org/10.1007/BF00384745

Pollard, P.J., Taylor, R.G. 2002. Paragenesis of the Grasberg Cu-Au deposit, Irian Jaya, Indonesia: results from logging section 13. *Mineralium Deposita*, **37**, 117–136, https://doi.org/10.1007/s00126-001-0234-7

Pollard, P.J., Taylor, R.G. and Peters, L. 2005. Ages of intrusion, alteration, and mineralization at the Grasberg Cu-Au deposit, Papua, Indonesia. *Economic Geology*, **100**, 1005–1020, https://doi.org/10.2113/gsecongeo.100.5.1005

Richards, J.P. 2011. High Sr/Y arc magmas and porphyry Cu ± Mo ± Au deposits: just add water. *Economic Geology*, **106**, 1075–1081, https://doi.org/10.2113/econgeo.106.7.1075

Sidorov, A.A. and Eremin, R.A. 1994. Metallogeny and gold lode deposits of northeastern Russia. *ICAM-94 Proceedings*, Belgorod, Russia, 247–256.

Sillitoe, R.H. 1972. A plate tectonic model for the origin of porphyry copper deposits. *Economic Geology*, **67**, 184–197, https://doi.org/10.2113/gsecongeo.67.2.184

Sillitoe, R.H. 1973. The tops and bottoms of porphyry copper deposits. *Economic Geology*, **68**, 799–815, https://doi.org/10.2113/gsecongeo.68.6.799

Sillitoe, R.H. 1979. Some thoughts on gold-rich porphyry copper deposits. *Mineralium Deposita*, **14**, 161–174, https://doi.org/10.1007/BF00202933

Sillitoe, R.H. 1997. Characteristics and controls of the largest porphyry copper-gold and epithermal gold deposits in the circum-Pacific region. *Australian Journal of Earth Sciences*, **44**, 373–388, https://doi.org/10.1080/08120099708728318

Sillitoe, R.H. 2002. Some metallogenic features of gold and copper deposits related to alkaline rocks and consequences for exploration. *Mineralium Deposita*, **37**, 4–13 https://doi.org/10.1007/s00126-001-0227-6

Sokolov, S.D. 2010. Tectonics of Northeast Asia: an overview. *Geotectonics*, **44**, 493–509, https://doi.org/10.1134/S001685211006004X

Sokolov, S.D., Ledneva, G.V., Tuchkova, M.I., Luchitskaya, M.V., Ganelin, A.V. and Verzhbitsky, V.E. 2011. Chukchi arctic continental margins: tectonic evolution, link to the opening of the America–Asia Basin. *ICAM VI Proceedings of the International Conference on Arctic Margins VI Fairbanks*, AK, May 2011, 97–113.

Sokolov, S.D., Tuchkova, M.I., Ganelin, A.V., Bondarenko, G.E. and Layer, P. 2015. Tectonics of the South Anyui Suture, Northeastern Asia. *Geotectonics*, **49**, 3–26, https://doi.org/10.1134/S0016852115010057

Soloviev, S.G. 2014. *The Metallogeny of Shoshonitic Magmatism*, **1**. Scientific World, Moscow.

Stern, C.R., Funk, J.A., Skewes, M.A. and Arévalo, A. 2007. Magmatic anhydrite in plutonic rocks in the El Teniente porphyry Cu–Mo deposit, Chile, and the role of sulfur- and copper-rich magmas in its formation. *Economic Geology*, **102**, 1335–1344, https://doi.org/10.2113/gsecongeo.102.7.1335

Tikhomirov, P.L., Kalinina, E.A., Moriguti, T., Makishima, A., Kobayashi, K., Cherepanova, I.Y. and Nakamura, E. 2012. The Cretaceous Okhotsk–Chukotka volcanic belt (NE Russia): geology, geochronology, magma output rates, and implications on the genesis of silicic LIPs. *Journal of Volcanology and Geothermal Research*, **222**, 14–32, https://doi.org/10.1016/j.jvolgeores.2011.12.011

Tikhomirov, P.L., Prokof'ev, V.Yu., Kal'ko, I.A., Apletalin, A.V., Nikolaev, Yu.N., Kobayashi, K. and Nakamura, E. 2017. Post-collisional magmatism of Western Chukotka and Early Cretaceous tectonic rearrangement in northeastern Asia. *Geotectonics*, **51**:131–151, https://doi.org/10.1134/S0016852117020054

Titley, S.R. 1972. Intrusion and wall rock, porphyry copper deposits. *Economic Geology*, **67**, 122–123, https://doi.org/10.2113/gsecongeo.67.1.122

Titley, S.R. 1975. Geological characteristics and environment of some porphyry copper occurrences in the southwestern Pacific. *Economic Geology*, **70**, 499–514, https://doi.org/10.2113/gsecongeo.70.3.499

Titley, S.R. 1981. Porphyry copper: circumstantial evidence suggests that porphyry-related deposits, currently the world's principal source of copper, may have formed as by-products of volcanic activity. *American Scientist*, **69**, 632–638.

Volchkov, A.G., Sokirkin, G.I. and Shishakov, V.B. 1982. Geological setting and ore composition of the Anyuiskoe porphyry copper deposit. *Geologia Rudnykh Mestorozhdenii*, **4**, 89–94 [in Russian].

Volkov, A.V., Savva, N.E., Sidorov, A.A., Egorov, V.N., Shapovalov, V.S., Prokof'ev, V.Y. and Kolova, E.E. 2006. Spatial distribution and formation conditions of Au-bearing porphyry Cu–Mo deposits in the northeast of Russia. *Geology of Ore Deposits*, **48**, 448–472, https://doi.org/10.1134/S107570150606002X

Winchester, J.A. and Floyd, P.A. 1977. Geochemical discrimination of different magma series and their differentiation products using immobile elements. *Chemical Geology*, **20**, 325–343, https://doi.org/10.1016/0009-2541(77)90057-2

Yang, Z., Hou, Z., White, N.C., Chang, Z., Li, Z. and Song, Y. 2008. Geology of the post-collisional porphyry copper–molybdenum deposit at Qulong, Tibet. *Ore Geology Reviews*, **36**, 133–159, https://doi.org/10.1016/j.oregeorev.2009.03.003

Zajacz, Z., Seo, J.H., Candela, P.A., Piccoli, P.M., Heinrich, C.A. and Guillong, M. 2010. Alkali metals control the release of gold from volatile-rich magmas. *Earth and Planetary Science Letters*, **297**, 50–56, https://doi.org/10.1016/j.epsl.2010.06.002

Zheng, Y.C., Wu, C.D., Tian, S.H., Hou, Z.Q., Fu, Q. and Zhu, D.C. 2020. Magmatic and structural controls on the tonnage and metal associations of collision-related porphyry copper deposits in southern Tibet. *Ore Geology Reviews*, **122** (in press) https://doi.org/10.1016/j.oregeorev.2020.103509

Zhong, S., Feng, C., Seltmann, R. and Dai, Z. 2018. Geochemical contrasts between late Triassic ore-bearing and barren intrusions in the Weibao Cu–Pb–Zn deposit, east Kunlun Mountains, NW China: constraints from accessory minerals (zircon and apatite). *Mineralium Deposita*, **53**, 855–870, https://doi.org/10.1007/s00126-017-0787-8